BASS. XXVI. DR2 host galaxy stellar velocity dispersions

Koss, M.J.; Trakhtenbrot, B.; Ricci, C.; Oh, K.; Bauer, F.E.; Stern, D.; ... ; Urry, C.M.

The Astrophysical Journal Supplement Series, 261:6 (26pp), 2022 July https://doi.org/10.3847/1538-4365/ac650b

BASS. XXVI. DR2 Host Galaxy Stellar Velocity Dispersions

Michael J. Koss[1,2], Benny Trakhtenbrot[3], Claudio Ricci[4,5], Kyuseok Oh[6,7,28], Franz E. Bauer[2,8,9], Daniel Stern[10], Turgay Caglar[11], Jakob S. den Brok[12,13], Richard Mushotzky[14], Federica Ricci[15,16], Julian E. Mejía-Restrepo[17], Isabella Lamperti[18], Ezequiel Treister[19], Rudolf E. Bär[12], Fiona Harrison[20], Meredith C. Powell[21], George C. Privon[22,23], Rogério Riffel[24], Alejandra F. Rojas[25], Kevin Schawinski[26], and C. Megan Urry[27]

[1] Eureka Scientific, 2452 Delmer Street, Suite 100, Oakland, CA 94602-3017, USA; mike.koss@eurekasci.com
[2] Space Science Institute, 4750 Walnut Street, Suite 205, Boulder, CO 80301, USA
[3] School of Physics and Astronomy, Tel Aviv University, Tel Aviv 69978, Israel
[4] Núcleo de Astronomía de la Facultad de Ingeniería, Universidad Diego Portales, Av. Ejército Libertador 441, Santiago 22, Chile
[5] Kavli Institute for Astronomy and Astrophysics, Peking University, Beijing 100871, People's Republic of China
[6] Korea Astronomy & Space Science Institute, 776, Daedeokdae-ro, Yuseong-gu, Daejeon 34055, Republic of Korea
[7] Department of Astronomy, Kyoto University, Kitashirakawa-Oiwake-cho, Sakyo-ku, Kyoto 606-8502, Japan
[8] Instituto de Astrofísica and Centro de Astroingeniería, Facultad de Física, Pontificia Universidad Católica de Chile, Casilla 306, Santiago 22, Chile
[9] Millennium Institute of Astrophysics (MAS), Nuncio Monseñor Sótero Sanz 100, Providencia, Santiago, Chile
[10] Jet Propulsion Laboratory, California Institute of Technology, 4800 Oak Grove Drive, MS 169-224, Pasadena, CA 91109, USA
[11] Leiden Observatory, PO Box 9513, 2300 RA, Leiden, The Netherlands
[12] Institute for Particle Physics and Astrophysics, ETH Zürich, Wolfgang-Pauli-Strasse 27, CH-8093 Zürich, Switzerland
[13] Argelander Institute for Astronomy, Auf dem Hügel 71, D-53231, Bonn, Germany
[14] Department of Astronomy, University of Maryland and Joint Space-Science Institute, College Park, MD 20742, USA
[15] Dipartimento di Fisica e Astronomia, Università di Bologna, via Gobetti 93/2, I-40129 Bologna, Italy
[16] INAF Osservatorio Astronomico di Bologna, via Gobetti 93/3, I-40129 Bologna, Italy
[17] European Southern Observatory, Casilla 19001, Santiago 19, Chile
[18] Centro de Astrobiología (CAB), CSIC-INTA, Cra. de Ajalvir Km. 4, E-28850 Torrejón de Ardoz, Madrid, Spain
[19] Instituto de Astrofísica, Facultad de Física, Pontificia Universidad Católica de Chile, Casilla 306, Santiago 22, Chile
[20] Cahill Center for Astronomy and Astrophysics, California Institute of Technology, Pasadena, CA 91125, USA
[21] Kavli Institute of Particle Astrophysics and Cosmology, Stanford University, 452 Lomita Mall, Stanford, CA 94305, USA
[22] National Radio Astronomy Observatory, 520 Edgemont Road, Charlottesville, VA 22903, USA
[23] Department of Astronomy, University of Florida, P.O. Box 112055, Gainesville, FL 32611, USA
[24] Departamento de Astronomia, Instituto de Física, Universidade Federal do Rio Grande do Sul, CP 15051, 91501-970, Porto Alegre, RS, Brazil
[25] Centro de Astronomía (CITEVA), Universidad de Antofagasta, Avenida Angamos 601, Antofagasta, Chile
[26] Modulos AG, Technoparkstrasse 1, CH-8005 Zurich, Switzerland
[27] Yale Center for Astronomy & Astrophysics, Physics Department, PO Box 208120, New Haven, CT 06520-8120, USA
Received 2022 January 12; revised 2022 February 11; accepted 2022 February 16; published 2022 July 15

Abstract

We present new central stellar velocity dispersions for 484 Sy 1.9 and Sy 2 from the second data release of the Swift/BAT AGN Spectroscopic Survey (BASS DR2). This constitutes the largest study of velocity dispersion measurements in X-ray-selected obscured active galactic nuclei (AGN) with 956 independent measurements of the Ca II H and K λ3969, 3934 and Mg I λ5175 region (3880–5550 Å) and the calcium triplet region (8350–8730 Å) from 642 spectra mainly from VLT/X-Shooter or Palomar/DoubleSpec. Our sample spans velocity dispersions of 40–360 km s^{1}, corresponding to 4–5 orders of magnitude in black hole mass ($M_{\rm BH} = 10^{5.5-9.6}\ M_{\odot}$), bolometric luminosity ($L_{\rm bol} \sim 10^{42-46}$ erg s^{-1}), and Eddington ratio ($L/L_{\rm Edd} \sim 10^{-5}$ to 2). For 281 AGN, our data and analysis provide the first published central velocity dispersions, including six AGN with low-mass black holes ($M_{\rm BH} = 10^{5.5-6.5}\ M_{\odot}$), discovered thanks to high spectral resolution observations ($\sigma_{\rm inst} \sim 25$ km s^{-1}). The survey represents a significant advance with a nearly complete census of velocity dispersions of hard X-ray–selected obscured AGN with measurements for 99% of nearby AGN ($z < 0.1$) outside the Galactic plane ($|b| > 10°$). The BASS AGN have much higher velocity dispersions than the more numerous optically selected narrow-line AGN (i.e., ∼150 versus ∼100 km s^{-1}) but are not biased toward the highest velocity dispersions of massive ellipticals (i.e., >250 km s^{-1}). Despite sufficient spectral resolution to resolve the velocity dispersions associated with the bulges of small black holes ($\sim 10^{4-5}\ M_{\odot}$), we do not find a significant population of super-Eddington AGN. Using estimates of the black hole sphere of influence from velocity dispersion, direct stellar and gas black hole mass measurements could be obtained with existing facilities for more than ∼100 BASS AGN.

Unified Astronomy Thesaurus concepts: Supermassive black holes (1663); X-ray surveys (1824); Sky surveys (1464); X-ray active galactic nuclei (2035); AGN host galaxies (2017)

Supporting material: machine-readable tables

1. Introduction

Over the last two decades, dedicated surveys have established several scaling relations between supermassive black hole (SMBH) mass ($M_{\rm BH}$) and host galaxy properties, including the bulge luminosity and mass ($M_{\rm bulge}$), stellar velocity dispersion inferred from spectral absorption lines (σ_*), concentration index,

[28] JSPS Fellow.

and Sérsic index (see, e.g., the review by Kormendy & Ho 2013, and references therein). These scaling relations strongly support a picture in which SMBHs and their host galaxies "coevolve," in the sense that the growth histories of the two components are physically interlinked, perhaps through some form of SMBH-related feedback mechanism (see, e.g., the review by Fabian 2012, and references therein).

Observationally, the tightest and perhaps most robust link between SMBHs and their hosts is the $M_{\rm BH}$–σ_* scaling relation (e.g., <0.5 dex; Marsden et al. 2020). Calibrating this relation has relied on a rather modest number (e.g., $N = 145$; Sahu et al. 2019a, 2019b) of direct $M_{\rm BH}$ measurements with varying precision from stellar or gas dynamics, kinematics of megamasers, proper motion, or recent direct-imaging techniques. The spatially resolved measurements of stellar and/or gas dynamics comprise the majority of these measurements and typically require very high spatial resolutions that are possible only for the nearest galaxies (e.g., McConnell & Ma 2013). Encouragingly, the high resolution offered by the Atacama Large Millimeter/submillimeter Array (ALMA) is increasingly being used to this end for nearby galaxies, tracking the dynamics of the circumnuclear gas dynamics as it is strongly affected by the SMBH gravitational field (e.g., Cohn et al. 2021). Other direct measurements, such as using H_2O megamasers, are only possible for a small number of galaxies with favorable alignments (Greene et al. 2016).

Using these direct measurements, various studies have suggested systematic environmental differences or possible selection biases in the $M_{\rm BH}$–σ_* relation in elliptical (typically higher mass) and spiral (typically lower mass) morphological galaxy types, barred galaxies, and pseudobulges (e.g., Graham 2008; Greene et al. 2016; Shankar et al. 2017). Other studies have suggested variations of σ_* due to spectral regions probing different stellar populations (e.g., Riffel et al. 2015). Notwithstanding these limitations and possible biases, the $M_{\rm BH}$–σ_* relation has been found to extend unbroken down to $M_{\rm BH} \sim 10^5\ M_\odot$ (although with increasing scatter; e.g., Greene et al. 2020) and seems to be the most fundamental relation between SMBHs and their host galaxies (e.g., van den Bosch et al. 2015; Shankar et al. 2019). This, in turn, makes it useful for inferring $M_{\rm BH}$ in much larger samples of galaxies.

Active galactic nuclei (AGN) provide the best tracer of SMBH accretion throughout cosmic time. Although technically challenging in the presence of (optical) AGN contamination (e.g., Greene & Ho 2006), velocity dispersion measurements have been obtained for various AGN populations, including unobscured broad-line AGN (type 1 AGN, hereafter Sy 1) to calibrate so-called "virial" $M_{\rm BH}$ estimators (e.g., Grier et al. 2013; Woo et al. 2013); AGN in dwarf galaxies, which probe the low-mass end of the "coevolutionary" picture (e.g., Martin-Navarro & Mezcua 2018; Baldassare et al. 2020); and obscured narrow-line AGN (type 2, hereafter Sy 2 sources; e.g., Garcia-Rissmann et al. 2005). Among the many ways to survey the AGN population, hard X-rays (>2 keV) provide the most complete census for distant, strongly accreting AGN (see, e.g., Brandt & Hasinger 2005), as a large fraction—indeed, the majority—of the AGN population is obscured (see the review by, e.g., Hickox & Alexander 2018). Ultrahard X-ray emission (>10 keV) provides an even more complete tracer of the radiation from obscured AGN (i.e., an equivalent neutral hydrogen absorbing column, $N_{\rm H} > 10^{22}\,{\rm cm}^{-2}$), probing into the Compton-thick (CT) regime (i.e., $N_{\rm H} > 10^{24}\,{\rm cm}^{-2}$; see, e.g., Ricci et al. 2015; Koss et al. 2016a). Ultimately, studying the stellar velocity dispersion of a large sample of nearby ultrahard X-ray–selected AGN is crucial to get good constraints on σ_* in obscured AGN and thus the SMBH mass distribution among this population and serves as a critical nearby benchmark for high-redshift AGN, where host galaxy velocity dispersions are difficult to measure.

Despite the importance of central (e.g., $\lesssim$kpc) velocity dispersions for inferring $M_{\rm BH}$ in obscured AGN, relatively few large studies (i.e., >100 systems) have been performed, mostly within the context of large-scale surveys of galaxies such as the Sloan Digital Sky Survey (SDSS; e.g., Greene & Ho 2005; Thomas et al. 2013). Compared to obscured (narrow-line) AGN selected via strong line ratio diagnostics from the SDSS (e.g., [O III] $\lambda5007/{\rm H}\beta$ versus [N II] $\lambda6583/{\rm H}\alpha$; Baldwin et al. 1981; Veilleux & Osterbrock 1987; Kewley et al. 2001), ultrahard X-ray–selected AGN are sometimes missed due to being in significantly more dusty host galaxies (e.g., Koss et al. 2017) with higher star formation rates (e.g., Koss et al. 2013, 2021). Thus, surveying the velocity dispersions of ultrahard X-ray–selected AGN host galaxies offers an important complement to optical surveys.

The goal of the BAT AGN Spectroscopic Survey[29] (BASS) is to generate the largest available optical spectroscopic data set for the sample of Swift/BAT ultrahard X-ray (14–195 keV) detected AGN. As part of this effort, the first data release (DR1) of BASS (Koss et al. 2017) used mostly archival optical spectra for 641 AGN from the 70 month BAT catalog (Baumgartner et al. 2013) to derive central velocity dispersions for 202 AGN. The DR1 found that BAT AGN tend to have larger central velocity dispersions than SDSS-selected, narrow-line Sy 2 AGN. Notably, almost all of the DR1 observations were obtained with smaller (1.5–2.5 m) telescopes spread across various surveys and other past studies, each using bespoke reduction routines, leading to substantial inhomogeneity in quality and parameter constraints. Importantly, many BASS DR1 spectra also had spectral resolutions that were too low ($R < 1000$) to robustly measure the stellar velocity dispersion in low-mass AGN ($M_{\rm BH} \lesssim 10^7\ M_\odot$).

In this paper, part of the BASS DR2 Special Issue, we greatly improve upon the DR1 results by presenting and analyzing targeted observations of central velocity dispersions for a nearly complete sample of AGN ($\geqslant$95%) drawn from the 70 month BAT catalog with higher spectral resolution and signal-to-noise ratios (S/Ns). We focus on a complete sample of Sy 1.9 and Sy 2, where these measurements can be made in the absence of significant AGN contamination based on a large number of new, high-quality spectra. A more detailed study of the nearest ($z < 0.01$) 19 local luminous AGN within the 70 month Swift/BAT catalog is provided in Caglar et al. (2020). Another complementary DR2 study (T. Caglar et al. 2022, in preparation) will focus on the velocity dispersions of the broad-line Sy 1 AGN (with broad Hβ, e.g., FWHM >1000 km s^{-1}) in the same parent sample.

An overview of the BASS DR2 spectroscopic sample used in this work is provided in Koss et al. (2022a), while full details of the 858 AGN, including revised counterparts, classifications, observations, and reductions, are in Koss et al. (2022b). Broad emission line measurements for the BASS DR2 sample are presented in Mejía-Restrepo et al. (2022), while narrow-line

[29] https://www.bass-survey.com/

measurements are presented in Oh et al. (2022). Ananna et al. (2022) used the highly complete set of BASS DR2 measurements to derive the intrinsic X-ray luminosity function, black hole (BH) mass function, and Eddington ratio distribution function for both obscured and unobscured low-redshift AGN, relying on the σ_* measurements presented here (for narrow-line systems). Completing the DR2 Special Issue, the details of the DR2 near-infrared (NIR) spectroscopy are provided in den Brok et al. (2022), with an investigation of NIR coronal lines. The NIR emission from broad-line regions and associated virial SMBH mass estimates are studied in Ricci et al. (2022). Finally, Pfeifle et al. (2022) investigated the relationship between mid-IR colors and X-ray column density.

Throughout this work, we adopt $\Omega_M = 0.3$, $\Omega_\Lambda = 0.7$, and $H_0 = 70\,\mathrm{km\,s^{-1}\,Mpc^{-1}}$. To determine the extinction due to Milky Way foreground dust, we use the maps of Schlegel et al. (1998) and the extinction law derived by Cardelli et al. (1989). For consistency with the BASS DR1 (Koss et al. 2017), we define Sy 1 as AGN with broad Hβ line emission, Sy 1.9 as having narrow Hβ and broad Hα, and Sy 2 AGN as having both narrow Hβ and narrow Hα (this latter category includes small numbers of LINERs and AGN in star formation–dominated galaxies).

2. AGN Spectroscopic Sample and Data

The goal of the BASS DR2 is to provide a complete sample of SMBH mass estimates and multiwavelength ancillary measurements using targeted observations for all AGN in the 70 month Swift/BAT survey. The optical spectroscopy component focuses on either broad emission lines (mostly Balmer lines) or (host galaxy) stellar velocity dispersion measurements to obtain SMBH estimates while also covering the broadest possible spectral range (i.e., within the accessible visual range, 3200–10000 Å) for emission line measurements for the entire catalog of 858 AGN. We discuss the obscured AGN sample along with some aspects of the parent optical spectra sample below and refer the reader to the DR2 overview (Koss et al. 2022a) and the detailed catalog paper (Koss et al. 2022b) for more details.

2.1. AGN Sample

The AGN sample starts with the 858 AGN listed in the 70 month BAT catalog that comprise the BASS DR2 (Koss et al. 2022b). As stellar velocity dispersions are difficult (or impossible) to measure when the spectrum is dominated by AGN continuum emission, we excluded from our sample 106 beamed and/or lensed AGN and 359 AGN with broad Hβ based on the classifications from Mejía-Restrepo et al. (2022), as these have broad line–based mass estimates. A separate investigation of velocity dispersions in a subset of BASS DR2 Sy1 systems was carried out by T. Caglar et al. (2022, in preparation), where special care is taken to tackle the AGN contamination. This leaves 393 Sy 1.9 and Sy 2 AGN from the parent DR2 sample of 858 AGN (i.e., 46%, 393/858). For potential dual AGN in the sample (e.g., Koss et al. 2011b, 2012, 2015, 2016b), each AGN is only included in the sample if X-ray detected and bright enough to be detected individually by Swift/BAT. From this parent sample of 393 obscured DR2 AGN, we were able to successfully measure σ_* in 359 AGN.

The velocity measurements described below were also carried out successfully on 125 additional obscured AGN from the deeper 105 month Swift/BAT all-sky survey (e.g., Oh et al. 2018) collected as part of the ongoing BASS efforts. As counterpart identification is still ongoing for the 105 month sample, we stress that this sample is neither complete nor final and does not represent a flux- or volume-complete subset of the deeper BAT data. Thus, we omit this additional bonus sample when discussing completeness measurements. So the final obscured AGN sample totals 484 from 359 DR2 and 125 bonus 105 month AGN.

2.2. Sample of Spectra

Our sample starts from 960 BASS spectra of the Sy 1.9 and Sy 2 AGN from the 70 month AGN catalog (for a review, see Koss et al. 2022b) and additional obscured AGN from the deeper 105 month. The majority of the spectra (67%, 651/960) are newly obtained from the Very Large Telescope (VLT) using the X-Shooter instrument, a multiwavelength (3000–25000 Å) echelle spectrograph (Vernet et al. 2011), or from the DoubleSpec (DBSP) instrument mounted on the 200 inch telescope at Palomar Observatory. The VLT/X-Shooter consists of three spectroscopic arms covering the ultraviolet blue (UVB; 3000–5595 Å), visual (VIS; 5595–10240 Å), and NIR (10240–24800 Å). The spectra also include significant new data sets from the Southern Astrophysical Research (SOAR) telescope using the Goodman High Throughput Spectrograph (Clemens et al. 2004). Finally, legacy SDSS spectra are used when available, as well as smaller contributions from other telescopes.

Importantly for the construction of the sample and data set used in the present work, we note that repeated observations of these AGN were carried out if either the S/N over the spectral features relevant for the detailed measurements and/or the spectral resolution was too low to robustly measure the stellar absorption features (i.e., $\Delta\sigma_* > 20$ km s^{-1}). Specifically, high spectral resolution observations (i.e., $\sigma_{\rm inst} \approx 25$ km s^{-1}), even if over a limited spectral range, were pursued primarily for obscured AGN (Sy 1.9 and Sy 2), for which stellar velocity measurements provide the only way to estimate BH masses. Additional repeated observations of spectra were also sometimes attempted to improve the accuracy of σ_* for lower-quality measurements (10 km s^{-1} $< \Delta\sigma_* <$ 20 km s^{-1}).

Outside of the SDSS sample, which was in both the DR1 and DR2, almost all of the DR1 spectra were reobserved with larger telescopes at much higher quality and spectral resolution, so we do not include them in this analysis. We do, however, include a sample of 21 high-quality spectra from the DR1 from Gemini. For sample completeness, we also include a single DR1 spectrum of M81, a very bright and nearby galaxy, which was not part of the DR2 release due to instrumental issues. After including these samples, only 35 spectra remain with acceptable velocity dispersions ($\Delta\sigma_* < 20$ km s^{-1}) from the DR1, all of which were reobserved in the DR2, so we do not remeasure the remaining DR1 spectra in this release.

Throughout the text, due to the frequent duplications of AGN spectra from different telescopes and from the same telescope using a higher-resolution setup, we use the nomenclature "best" to refer to the spectra with the lowest velocity dispersion error in kilometers per second in either the 3880–5550 Å region or the 8350–8730 Å fitting region. In other words, for an individual AGN, we compare the $\Delta\sigma_*$ of

Table 1
Summary of BASS Spectra Used

Telescope (1)	Instrument (2)	N_{best} (3)	$N_{sec.}$ (4)	λ_{range} (Å) (5)	Slit Width (arcsec) (6)	R_{5000} (7)	R_{8500} (8)
VLT	X-Shooter	163	21	2990–10200	1.5	3850	6000
Palomar[a]	DBSP	101	61	3150–10500	1.5	1220	1730
		51	11	3970–5499/8050–9600	2	2170	4720
APO	SDSS	91	2	3830–9180	3	1760	2490
SOAR	Goodman	53	27	7900–9070	1.2	⋯	4720
		1	10	4560–8690	1.2	890	⋯
		1	4	5280–7900	1.2	1450	⋯
Keck	LRIS/DEIMOS	6	3	3200–10280	1	1280	1810
Magellan	MagE	6	1	3300–10010	1	3850[b]	⋯
VLT	MUSE	6	0	4800–9300	2[c]	1850	3150
VLT	FORS2	1	0	3400–6100	2	830	⋯
Gemini[d]	GMOS	3	18	4000–7000	1	1050	⋯
Perkins[e]	Deveny	1	0	3900–7500	2	920	⋯
Total		484	158				

Notes. The columns are as follows. (1) Telescope. (2) Instrument used. (3), (4) Whether the spectra were included in the best measurement or a secondary measurement. (5)–(8) The wavelength range, slit width, and resolving power at 5000 and 8500 Å, respectively. These represent typical values for this setup and may differ by small factors for a small number of spectra. In some cases, larger or smaller slit widths (e.g., 1.″5 vs. 2″) were used, resulting in different resolutions. Here R is given at 5000 and 8500 Å, depending on the spectral range. See Koss et al. (2022b) for a detailed list of instrument setups.
[a] There were two spectral setups used for Palomar, one at lower resolution for general observations of AGN and another in higher-resolution mode for velocity dispersions.
[b] The CaT region was not measured in Magellan/MagE spectra due to strong instrumental fringing.
[c] A 2″ diameter central aperture was extracted from the VLT/MUSE observation, except for NGC 6240, a close dual AGN where a 1″ aperture was used for each AGN.
[d] These Gemini spectra were used from the BASS DR1 because of their typically high S/N but are not part of the DR2.
[e] This BASS DR1 spectrum was used because the bright galaxy M81 was not part of the DR2 due to instrumental issues with sky subtraction.

all of the measurements from all of the spectra, and the best spectrum is the one that has the single lowest measurement error in a single region. We also include unique "secondary" spectra of the same AGN observed with a different telescope or instrumental setting, which have the second-lowest errors of any spectra, to enable a robust comparison between measurements to better understand issues like apertures, stellar libraries, instrumental issues, different fitting regions, etc., but we do not include these spectra for further scientific analysis in the paper. We exclude additional "tertiary" or even "quaternary" BASS spectra of 30 AGN of even worse quality to avoid biasing the results.

From the sample of 960 BASS spectra (and 22 DR1 spectra) of the 484 Sy 1.9 and Sy 2 AGN, we excluded 340 due to low-quality measurements or duplications. In total, 265 were excluded due to large errors in measurement ($\Delta\sigma_* > 20$ km s^{-1}), 45 due to velocity dispersions close to or below the instrumental resolution, and 30 due to tertiary or quaternary quality measurements. This leaves 484 best-fit spectra (and 158 secondary spectra).

A full summary of the best and secondary spectra and instrumental setups used specifically for velocity dispersion measurements is provided in Table 1. A summary of the redshift distribution, slit size in kiloparsecs, and instrumental resolutions is provided in Figure 1. Further details of instrumental settings, reductions, and observing conditions are provided in Koss et al. (2022b). In brief, the data reduction and analysis of DR2 spectra used here maintain the uniform approach described in the initial DR1 paper (Koss et al. 2017). All new spectra are processed using the standard tasks for cosmic-ray removal, 1 day spectral extraction, wavelength, and flux calibrations in either IRAF or the ESO/Reflex environment for the VLT instruments. The spectra are flux calibrated using standard stars, which were typically observed two to three times per night. The spectra are corrected for Galactic reddening. Finally, a telluric absorption correction is applied to the spectra with the software molecfit (i.e., for the 8350–8730 Å region). The instrumental resolution and line-spread function for each spectral setup were measured using the best estimate from telluric features (i.e., for the 8350–8730 Å region) when possible or Galactic stars observed as close in time as possible (i.e., for the 3880–5550 Å region, where strong telluric features are not present).

3. Velocity Dispersion Measurements

Here we provide an overview of the technique we use to measure stellar velocity dispersions (σ_*) for the AGN hosts in our sample. We discuss the specifics of the fitting regions and template library, the fitting technique and software, and masked regions.

3.1. Wavelength Regions and X-Shooter Spectral Library

In the BASS DR1, we used stellar population synthesis models from the Miles Indo-U.S. Catalog library of stellar spectra (Vazdekis et al. 2012) with a spectral resolution of 2.51 Å FWHM ($R \sim 2000$) and fitted the 3900–7000 Å range to measure the velocity dispersion using the Ca II H and K λ3969, 3934, the G band (at ∼4300 Å), and Mg I b λ5183, 5172, 5167 triplet absorption lines. We also used the 8350–8730 Å region to measure the Ca II λ8498, 8542, 8662 triplet (hereafter CaT). For BASS DR2, many sources were studied at much higher spectral resolutions (i.e., $R \gtrsim 5000$; particularly with VLT/X-Shooter); therefore, an updated library was needed to exploit

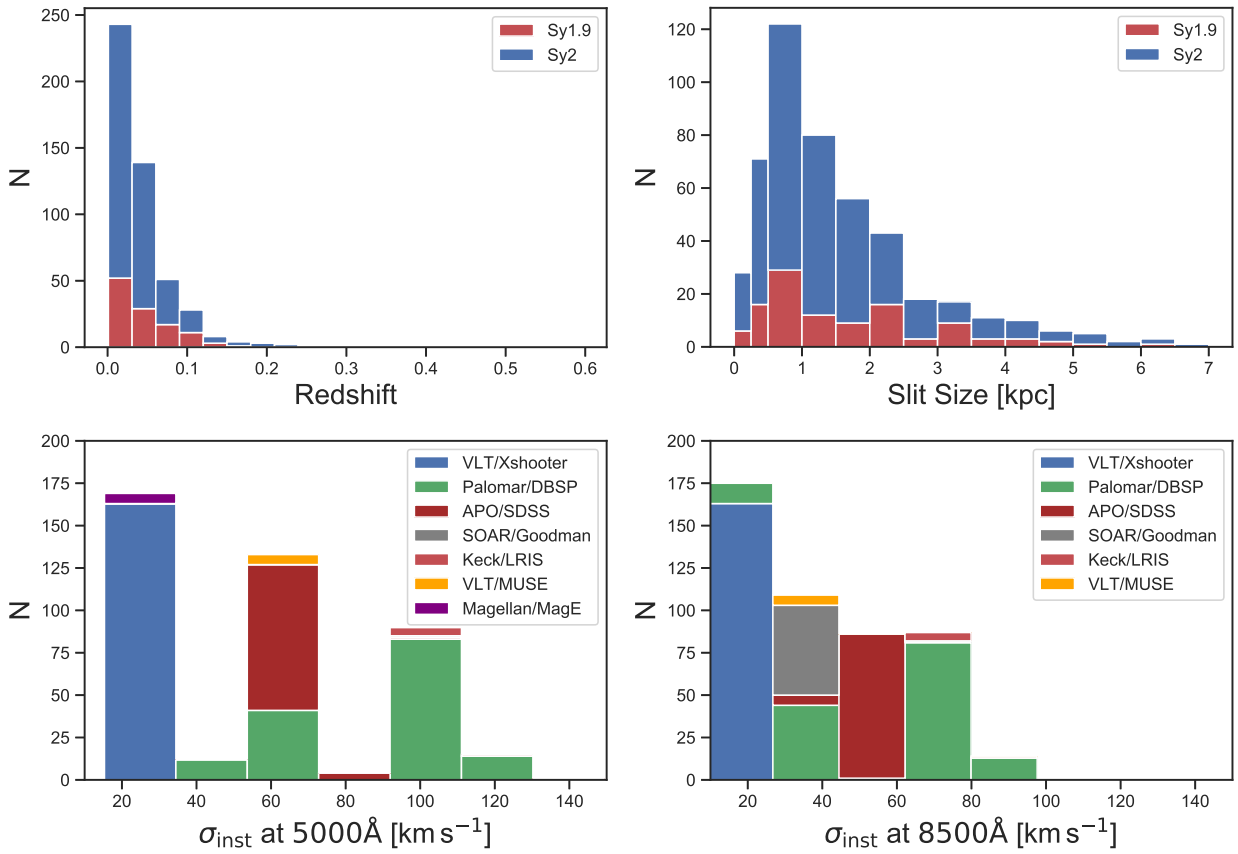

Figure 1. Summary of the AGN and the different observing conditions for the best 484 spectra in the sample. Top left: redshift range of the AGN in the sample, split into Sy 1.9 and Sy 2. Top right: slit width size in kiloparsecs for our AGN (again split into Sy 1.9 and Sy 2 sources). Bottom panels: instrumental resolution at 5000 (left) and 8500 Å (right) for the best spectra, from which we successfully measured σ_* from the 3880–5550 Å or CaT spectral regions (respectively).

the full instrumental resolution and probe lower-mass systems (e.g., <65 km s^{-1}).[30] Many studies have demonstrated how template libraries have great difficulty precisely recovering a velocity dispersion below their nominal resolution (e.g., Boardman et al. 2016, 2017; Gannon et al. 2020). Therefore, for the BASS DR2 analysis, we used the X-Shooter Spectral Library (XSL, specifically the XSL DR2; Gonneau et al. 2020), which includes observations of 666 stars covering the wavelength range 3000–24500 Å at a spectral resolving power close to $R \approx 10{,}000$.[31]

As a further improvement over BASS DR1, we have revised the fitting regions to measure σ_* to be the 3880–5550 and 8350–8730 Å spectral bands. We specifically excluded the region between 5550 and 7000 Å due to the lack of strong stellar absorption features, residual telluric features in the spectra from the oxygen bands, and the presence of weak broad Hα in Sy 1.9 that is difficult to mask. Additionally, the majority of our spectra were obtained with either VLT/X-Shooter or Palomar/DBSP, and in both cases, our spectral setups are such that the blue arm ends at ∼5550 Å. Focusing our σ_* measurements on two distinct spectral bands thus avoids any systematics that could have resulted from the "stitching" of spectra from various arms. Our choice of spectral bands means we focus on the UVB and VIS regions of the XSL templates (regardless of the instrument used to obtain each BASS spectrum).

For the VLT/X-Shooter template sample, we began with only slit loss–corrected stars (Gonneau et al. 2020), which included 813 observations of 666 stars. We then used only the slit loss–corrected observations available from the website,[32] which included 628 and 718 observations for the UVB and VIS regimes, respectively. Because the wavelength grids of the template spectra vary due to barycentric velocity corrections and cover a much wider range than necessary, we interpolated all stellar templates to a common wavelength grid with $\Delta\lambda = 0.2$ Å, which is the native pixel sampling of X-Shooter in the UVB and VIS arms. This resampling was done while conserving flux using `SpectRes` (Carnall 2021).[33] We also limited the spectral range of the stellar templates to slightly exceed the spectral fitting regions we planned to use for velocity dispersion, to avoid any discontinuities at the edge of the spectra. In the blue (UVB) regime, the templates are cut to ≃3800–5552 Å (compared to the fitting range of 3880–5550 Å). The edge at 5552 Å is the native red limit of the UVB arm of X-Shooter. For the red (VIS) regime, we limited the templates to cover the CaT, i.e., 8300–8900 Å. Excluding the rest of the spectra also helped avoid issues with correction of the water vapor bands ($\sim 8100 < \lambda/\text{Å} < 8300$, $\sim 8930 < \lambda/\text{Å} < 9800$).

[30] A 2.51 Å FWHM for a template library corresponds to $\sigma = 64$ km s^{-1} at $\lambda = 5000$ Å.

[31] The X-Shooter instrument has a range of spectral setups; therefore, the XSL reaches a higher spectral resolution than our X-Shooter data.

[32] See http://xsl.u-strasbg.fr/page_dr2_all.html.

[33] https://spectres.readthedocs.io/en/latest/

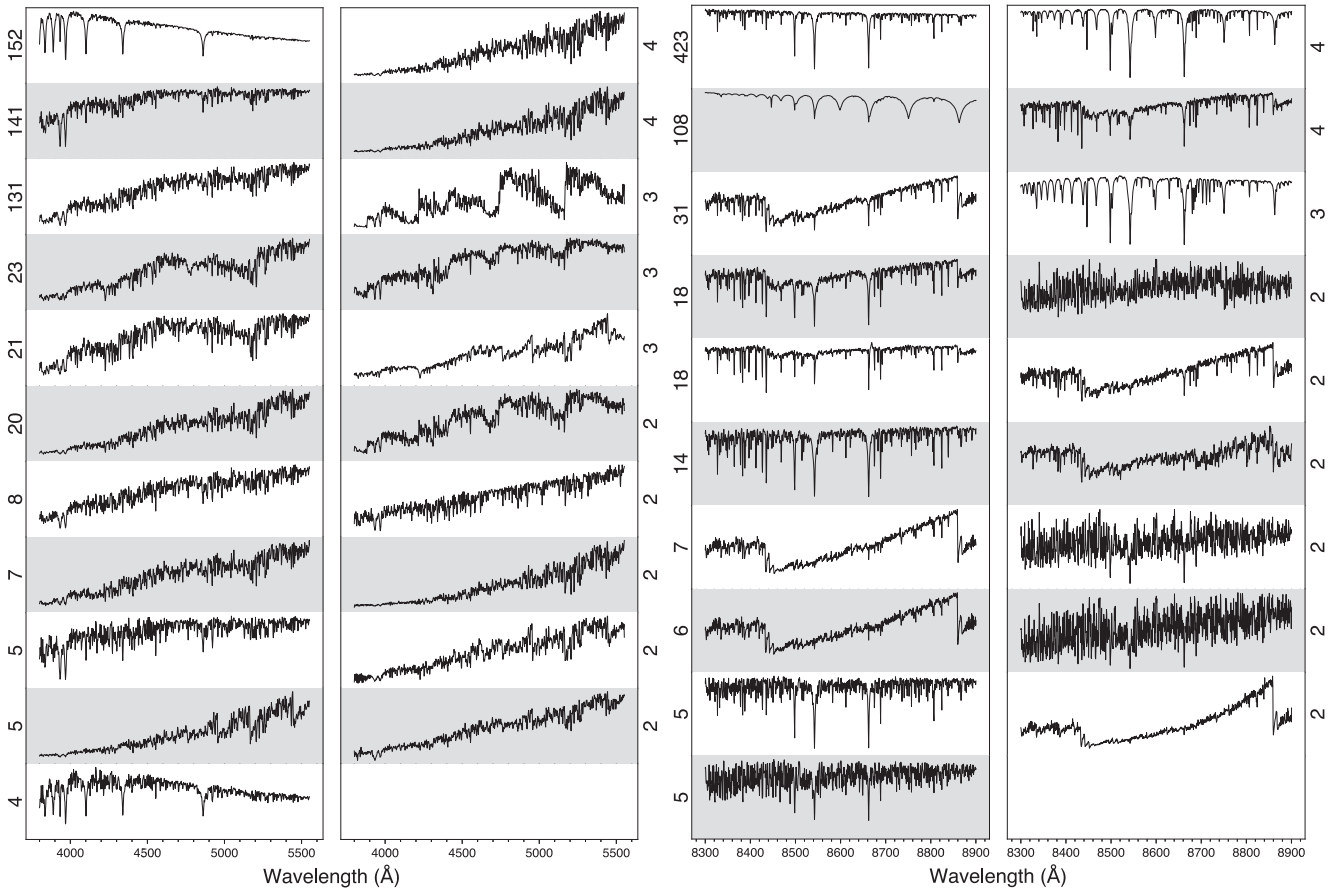

Figure 2. Examples of the X-Shooter stellar templates obtained via hierarchical clustering analysis and used in our work. Left: 21 blue (UVB) X-Shooter templates constructed from a subset of 628 X-Shooter stellar spectra, sorted by prominence in the spectral library (see Section 3.2). Right: 19 red (VIS) X-Shooter templates similarly constructed from a subset of 718 X-Shooter stellar spectra (see Section 3.2). The number next to the vertical axis of each template indicates the number of stellar spectra among the parent sample in which the features were found during the clustering analysis. All templates are shown in arbitrarily scaled units of F_λ.

3.2. Spectral Template Library from Hierarchical Clustering

When fitting spectra with template libraries, the execution time needed (per observed spectrum) scales roughly with the number of templates used and the number of spectral pixels. Thus, to facilitate the usage of large stellar libraries to fit galaxy spectra, smaller subsamples of stars are typically used. This is particularly important in our case, given the higher pixel sampling of some of our observations (e.g., 0.2 Å for VLT/X-Shooter) and our use of repeated bootstrap fitting for the error analysis as recommended by the penalized PiXel Fitting (`pPXF`) software (Cappellari 2017; see below).

We therefore proceeded with creating subsets of the stellar template library relying on cluster analysis, which is meant to identify groupings or clusters of similar objects (stellar spectra, in our case). This process also enables the identification and exclusion of any emission line features from flaring late-type stars, low-S/N features in only a single spectrum in the sample, and any possible instrumental issues in the large X-Shooter library that might affect template fitting. We follow the approach of Westfall et al. (2019), who applied a hierarchical clustering approach (e.g., Johnson 1967) to the full MILES stellar library of 985 stars to create the 42 representative templates used in their study. Their approach was shown to reduce the execution time by a factor of 25 while only slightly affecting the measurements (the median and 68th percentile confidence intervals were $\Delta\sigma_{\rm obs} = 0.9^{+3.6}_{-4.1}$ and $\Delta V = -1.3^{+2.0}_{-1.8}$). We note that the Westfall et al. (2019) approach is particularly relevant for our needs, as it was designed to decompose the (spatially resolved) spectra of low-redshift galaxies as part of the SDSS-IV MaNGA project.

For our clustering analysis, we use the same Python software that Westfall et al. (2019) used with MILES, `speclus`.[34] We use as input the 628 UVB arm stellar spectra over the range of 3800–5552 Å. This reduces the number of templates from 628 to 97 representative templates. We further remove from this set 30 templates with emission lines, one template with instrumental issues, and 45 representative templates comprised solely of one individual spectrum of low S/N (see Appendix B for examples of the excluded templates). The remaining 21 X-Shooter templates (Figure 2) used here have features found in two up to 152 stellar spectra. While these 21 templates are half of what was used in the MILES-based library described in, e.g., Westfall et al. (2019; 21/42), we note that the fitting region, 3800–5552 Å, is much narrower than the one used with their MILES-based library (3525–7500 Å); moreover, 15/42 of these MILES stars show little or no blue emission below 5552 Å.

In the redder (VIS) part of our library, we start the analysis with 718 spectra in the 8300–8900 Å region. The clustering analysis reduces the number of templates from 718 down to 79 representative templates. We further exclude 41 templates with

[34] Available at https://github.com/micappe/speclus.

prominent emission features in Paschen transitions or over the CaT region, which are all found in only single spectra, and 16 templates of relatively low S/N that are only comprised of a single spectrum (see Appendix B for examples of the excluded templates). This leaves 19 VIS templates (Figure 2).

3.3. Fitting Technique

Like in the BASS DR1, we use the penalized pPXF (Cappellari & Emsellem 2004; Python version 7.4.3) to measure stellar kinematics and the central stellar velocity dispersion (σ_*). This method operates in pixel space and uses a maximum penalized likelihood approach for deriving the line-of-sight velocity distribution (LOSVD) from kinematic data (Merritt 1997). The pPXF software is extensively used in extragalactic surveys for σ_* measurements, which would make our results more directly comparable with other studies.

As a first step, the pPXF code creates a model galaxy spectrum $G_{\rm mod}(x)$ by convolving a template spectrum with a parameterized LOSVD. Then it determines the best-fitting parameters of the LOSVD by minimizing the value of χ^2, which measures the agreement between the model and the observed galaxy spectrum over the set of reliable data pixels used in the fitting process. Finally, pPXF uses the best-fit spectra to calculate the velocity dispersion after subtracting the instrumental resolution (in quadrature).

Within pPXF we use a fitting procedure based on the example developed for the SAURON project (Cappellari & Emsellem 2004) with a velocity scale ratio of 2 to sample the templates at twice the resolution of the observed spectra (VELSCALE = 2) with the standard four moments (MOMENTS = 4). We use additive (DEGREE = 8) and multiplicative (MDEGREE = 1) polynomials to develop the best composite stellar population to fit the galaxy continuum and absorption lines, correct for inaccuracies in spectral calibration, and make the fit insensitive to a specific reddening curve. Importantly, modifying the degrees of additive polynomials (e.g., with DEGREE = 4–12) and/or removing the multiplicative polynomial (i.e., MDEGREE = 0) does not significantly change the fitting results, implying that the latter are robust.

To estimate the uncertainty associated with each σ_* measurement, we conservatively use the error estimate by pPXF or an error estimated through bootstrapping, whichever is larger. To estimate the bootstrap error, we resample the residuals of the initial velocity dispersion fit to construct 10 mock spectra to perform 10 additional fits. In general, the error given by pPXF is larger than the bootstrap errors, except for a few cases of fitting the CaT region. In addition to the σ_* measurement, pPXF also provides accurate, absorption features–based redshift determinations. These are completely independent of the emission line–based redshift measurements reported and used in other BASS (DR2) works and may be useful for studying velocity offsets between gas and stars in the (hosts of) BASS AGN.

Given the range of quality in our spectra and the presence of repeated spectroscopy for some sources, we excluded any measurements with a >20 km s^{-1} error for which other velocity dispersion measurements existed within our sample. For completeness, we included measurements with errors between 20 and 30 km s^{-1} if no other measurements existed.

Studies have found that measurements below or near the instrumental resolution have significantly increased scatter and may also be overestimated (see Scott et al. 2018, where they suggest an 18% cut) because biases can extend above the instrumental resolution (e.g., 100 km s^{-1} with $\sigma_{\rm SDSS\ inst} = 70$ km s^{-1}; Belfiore et al. 2019). Based on these studies and due to the intrinsic uncertainty in measuring instrumental resolution (Koss et al. 2022b), we therefore conservatively exclude any measurements within 20% above the corresponding instrumental resolution based on previous studies.

As these limitations were realized during our observational campaigns, the number of AGN covered in our work is not reduced at all, as any galaxies with σ_* near or below the spectral resolution were reobserved with higher-resolution setups (e.g., where $\sigma_{\rm inst} \sim 25$ km s^{-1}). Specifically, 10 AGN from 16 spectra from either Gemini/GMOS or Palomar/DBSP fell into this category, but all were reobserved using higher-resolution setups from VLT/X-Shooter or Palomar/DBSP.

We chose not to apply aperture corrections (e.g., Jorgensen et al. 1995) to the central velocity dispersions to place them at the effective radius or correct for inclination effects related to galaxy orientation (e.g., Bellovary et al. 2014). At fixed aperture, an increasing part of the host bulge and disk is sampled in spectra at increasing distances (redshifts), possibly leading to larger observed velocity dispersions. The aperture corrections that are designed to overcome this effect act in opposite directions, depending on whether the galaxy morphology is early- or late-type (e.g., Falcon-Barroso et al. 2017). This is extremely challenging to apply to the host galaxies in our sample, which are predominantly massive spirals with high concentration indices (i.e., lenticulars; Koss et al. 2011a), as it is not clear whether to increase or decrease the measured σ_* for each galaxy under study. Another issue is the significant fraction of mergers (e.g., 24%; Koss et al. 2010, 2018) that may have velocity dispersions affected due to the oscillations of the stars in the two progenitor galaxies as they pass by each other and coalesce. However, simulations suggest that during the merger, the σ_* values do not fall below 70% or exceed 200% and are much more likely to fall near the equilibrium value (Stickley & Canalizo 2012). However, dust attenuation associated with the merger may increase the scatter. A detailed host morphological analysis is needed but is beyond the scope of DR2. Additionally, LOSVD can be broadened due to orientation-dependent disk rotation, which would result in a larger dispersion outside the central spheroid component (e.g., Caglar et al. 2020). Finally, other studies do not find a significant offset of the SMBH masses deduced from pPXF-measured, uncorrected σ_* compared to those deduced from broad emission lines (within BASS), suggesting that aperture and rotation corrections are unlikely to be a major issue, at least in a statistical sense (e.g., Ricci et al. 2022). Future studies within BASS using integral field units such as VLT/MUSE are currently ongoing (e.g., Kakkad et al. 2022) and will hopefully serve to address this particular issue.

3.4. Masked Regions

The spectral fitting procedure is significantly improved by masking out certain spectral regions that are dominated by prominent emission lines. A full list of all masked emission lines is given in Appendix A. For the normal mask, the width of these masks was set to 2500 km s^{-1}, except for the brightest Hβ, [O III] λ4959, and [O III] λ5007 lines, where the masked regions were set to 5000 km s^{-1} to account for any blueshifted or weak broad emission components. We did not find that a narrower mask significantly improved the fitting. In practice, pPXF automatically applies a mask for several bright emission

lines: Hδ, Hγ, Hβ, [O III] λ5007, and [O I] λ6300. We further masked out the regions around the Ca H λ3968 line because of overlap with the Hϵ λ3970 and [Ne III] λ3968 emission lines. Since the overlapping emission lines reduce the depth of the Ca H absorption line, we expect that pPXF will also underestimate the depth and width of the Ca K line and consequently affect the measurement of σ_* (see, e.g., Greene & Ho 2005). Finally, we also excluded a few other bright emission lines (e.g., flux >5% Hβ in bright AGN; Tran et al. 2000, see our Table 6) from the velocity dispersion fits.

To make sure that our spectral fits are not affected by any residual line emission, we visually inspected the goodness of fit in the (initial) pPXF fits, and masked additional spectral regions, of weaker emission lines, motivated by past observations of bright AGN (e.g., Osterbrock et al. 1990; Osterbrock & Fulbright 1996), and repeated our fits. Here the width of the mask was set to 1000 km s^{-1}. In the case of the CaT region (8350–8730 Å), the initial fit was done with no masking of emission lines. If emission lines were seen in the residuals, we masked the relevant weak transitions of [O I] λ6300, [Cl II], [Fe II], Pa12, and/or Pa11. Additionally, we also masked the observed-frame spectral region of 9300–9700 Å, which is affected by strong telluric features. This was particularly relevant for higher-redshift AGN ($0.065 < z < 0.09$), where these telluric features strongly limit our ability to recover the intrinsic spectra. At yet higher redshifts, $z > 0.09$, no CaT measurements were made.

4. Results

In this section, we present the velocity dispersion fit results, compare the measurements available for some of our AGN within the BASS DR2 data set and in other compilations to better understand the uncertainties, discuss issues related to sample (in)completeness, and present the inferred estimates of BH mass for our BASS AGN.

4.1. Velocity Dispersions

A full catalog of σ_* measurements for the best spectra of 484 unique BASS AGN is provided in Table 2. In addition, σ_* measurements derived from secondary spectra are provided in Table 7 (in Appendix C). Example velocity dispersion fits are shown in Figure 3. Each spectrum may have a 3880–5550 Å and/or CaT spectral region fit, depending on the spectral setup and the σ_* measurement error. Some instruments yielded only measurements of one spectral region. Specifically, spectra obtained with SOAR/Goodman cover only the CaT region, while spectra obtained with either Magellan/MagE or Gemini/GMOS only have the 3880–5550 Å region.

The distributions of the σ_* measurements and associated errors for all spectra are shown in Figure 4. The median velocity dispersions from the 3880–5550 Å region (173 km s^{-1}) are somewhat higher than those of the CaT region (144 km s^{-1}). This is due to the higher typical redshift of the AGN with σ_* measured from the 3880–5550 Å region (median $z = 0.042$) compared to those with a CaT-based measurement ($z = 0.024$) and because of the increasing difficulty (or impossibility) of fitting the CaT region for sources at $z > 0.065$ (due to telluric features).

In Figure 5, we compare the distributions of the (best) σ_* measurements for the Sy 1.9 ($N = 113$) and Sy 2 ($N = 371$) sources in our sample. Overall, the two subsamples are very similar, with a median σ_* of 153 ± 5 and 157 ± 3 km s^{-1} for the Sy 1.9 and Sy 2 systems, respectively.

4.1.1. Comparisons between Measurements

In Figure 6, we compare the σ_* measurements of AGN with multiple spectra within BASS (i.e., best and secondary), further split by the two fitting regions. We find that, in general, there is good agreement among the 3880–5550 Å region measurements, with a scatter of 27 km s^{-1} (i.e., rms of $\sigma_{\rm best} - \sigma_{\rm sec}$) and 7/69 (10%) sources, where the difference between the measurements exceeds 30 km s^{-1} beyond the 1σ error bars. For the CaT region, the scatter between measurements is slightly larger, 31 km s^{-1}, and there is indeed a larger number of sources with significant discrepancies (11%, 11/100). It is unclear if the slightly higher fraction of outliers compared to 3880–5550 Å is related to the smaller fitting region or possible undetected issues with telluric features. The corresponding median absolute deviation (MAD), which is a robust estimator that is more resilient to outliers than the standard deviation, is merely 20 and 14 km s^{-1} for the 3880–5550 Å and CaT regions, respectively.

We next compare our best σ_* values to the literature measurements of BASS AGN from other studies (Figure 7) to understand the importance of varying instrumental setups, slit sizes and apertures, fitting regions and software, and templates. We focus on comparisons with large studies of velocity dispersions for comparison with significant sample sizes ($N > 50$) with several overlapping AGN in our sample ($N > 5$). This includes an early study of 85 AGN (Nelson & Whittle 1995) with low spectral resolution ($\sigma_{\rm inst} = 80$–230 km s^{-1}), an atlas of CaT fits (Garcia-Rissmann et al. 2005) for 78 AGN ($\sigma_{\rm inst} = 60$ km s^{-1}), and 428 dwarf Seyfert nuclei (Ho & Kim 2009) from a Palomar survey ($\sigma_{\rm inst} = 42$–118 km s^{-1}). We also include overlapping AGN in the Hobby-Eberly Telescope Massive Galaxy Survey (HETMGS; van den Bosch et al. 2015), which is an optical long-slit spectroscopic survey of 1022 massive galaxies (and includes AGN) using the 10 m Hobby-Eberly Telescope at McDonald Observatory ($\sigma_{\rm inst} = 108$–180 km s^{-1}). We limit our comparison to measurements of similar quality ($\Delta\sigma_* < 20$ km s^{-1}), and if an AGN was observed by more than one of these studies, we use the one with the lowest error in velocity dispersion. The final list includes 51 overlapping BASS AGN taken from these four studies. The literature sample tends to have somewhat larger errors (other than the 10 m HETMGS sample), whereby the BASS median error is 4 km s^{-1} compared to 9 km s^{-1} in the corresponding literature sample. In 43/51 cases, the BASS measurements have equivalent or lower estimated errors.

We find a scatter of 28 km s^{-1} (again, in an rms sense), which is very similar to previously published comparisons between sets of σ_* measurements (e.g., 28 km s^{-1}; Ho et al. 2009). The corresponding MAD we find is, again, smaller, at 16 km s^{-1}. There are three (ID = 573, 245, 548) significant outliers (e.g., >30 km s^{-1} offset after including 1σ error bars) compared to a large study of massive galaxies by van den Bosch et al. (2015). Two of the three outliers (ID = 573 and 548) have some of the largest velocity dispersion errors (19 and 21 km s^{-1}, respectively) of the BASS sample. The most extreme outlier is ID = 548 (NGC 3718), with an offset of 91 km s^{-1} from the reported literature value. In terms of outliers, when comparing their survey of dwarf AGN to the literature, Ho et al. (2009) found 2% (5/286) with offsets of

Table 2
Best Spectral Measurements

BAT ID	Galaxy	DR2 Type	Tele./Inst.	Res. Blue (Å)	Res. Red (Å)	Mask	$z_{3880-5550\ Å}$ (km s^{-1})	$\sigma_{3880-5550\ Å}$ (km s^{-1})	z_{CaT} (km s^{-1})	σ_{CaT} (km s^{-1})
(1)	(2)	(3)	(4)	(5)	(6)	(7)	(8)	(9)	(10)	(11)
1	2MASX J00004876–0709117	Sy 1.9	APO/SDSS	2.9	⋯	n	11,561 ± 14	126 ± 6	11,557 ± 17	124 ± 7
4	2MASX J00032742+2739173	Sy 2	APO/SDSS	2.9	⋯	n	12,170 ± 15	146 ± 5	12,139 ± 18	
7	SDSS J000911.57–003654.7	Sy 2	APO/SDSS	3.0	⋯	n	22,497 ± 22	205 ± 12		
10	LEDA 1348	Sy 1.9	VLT/X-Shooter	1.3	1.4	n	29,488 ± 25	253 ± 14		
13	LEDA 136991	Sy 2	Palomar/DBSP	2.3	1.8	n			3837 ± 15	131 ± 8
17	ESO 112-6	Sy 2	SOAR/GMAN	2.7	⋯	w			8911 ± 16	147 ± 7
20	2MASX J00343284–0424117	Sy 2	Keck/LRIS	3.9	4.7	n	65,639 ± 31	294 ± 22		
24	Mrk 344	Sy 2	Palomar/DBSP	4.1	4.9	n	7768 ± 18	152 ± 10	7658 ± 14	121 ± 7
25	SWIFT J004039.9+244539	Sy 1.9	Palomar/DBSP	2.0	1.3	n	24,018 ± 16	134 ± 6	23,952 ± 23	177 ± 14
28	NGC 235A	Sy 1.9	SOAR/GMAN	2.7	⋯	w			6817 ± 13	200 ± 3
29	2MASX J00430184+3017195	Sy 2	Palomar/DBSP	4.1	4.9	n			15,310 ± 21	135 ± 17
31	MCG-2-2-95	Sy 2	VLT/X-Shooter	1.3	1.4	n	6008 ± 11	83 ± 1	6010 ± 11	99 ± 2
32	ESP 39607	Sy 2	VLT/X-Shooter	1.3	1.4	n	61,938 ± 43	269 ± 29		
33	Mrk 348	Sy 1.9	Palomar/DBSP	4.1	4.9	w			4676 ± 25	82 ± 21
37	2MASX J00520383–2723488	Sy 2	VLT/X-Shooter	1.3	1.4	n	23,599 ± 18	195 ± 10	23,626 ± 17	182 ± 15
44	2MASX J01003490–4752033	Sy 2	SOAR/GMAN	2.7	⋯	w			14,706 ± 15	160 ± 7
49	MCG-7-3-7	Sy 2	SOAR/GMAN	2.7	⋯	w			9211 ± 14	190 ± 7
50	ESO 243-26	Sy 2	VLT/X-Shooter	1.3	1.4	n	5915 ± 16	93 ± 8	5937 ± 15	104 ± 5
53	UM 85	Sy 2	VLT/X-Shooter	1.3	1.4	n	12,524 ± 15	140 ± 5	12,510 ± 15	145 ± 6
55	2MASX J01073963–1139117	Sy 2	Palomar/DBSP	4.1	4.9	n	14,353 ± 18	151 ± 9	14,315 ± 19	181 ± 15
57	3C 33	Sy 2	VLT/X-Shooter	1.3	1.4	n	18,289 ± 16	239 ± 7	18,274 ± 16	248 ± 11

Note. The columns are as follows. (1) BAT 70 month survey catalog ID (https://swift.gsfc.nasa.gov/results/bs70mon/). (2) Host galaxy. (3) AGN type based on optical spectroscopy including Sy 1.9 (narrow Hβ and broad Hα) and Sy 2 (narrow Hβ and Hα) from Koss et al. (2022b). (4) Observatory and instrument used. (5) and (6) Instrumental resolution FWHM in Å from the DR2 for the blue (3880–5550 Å) and/or red (CaT) region. (7) Emission line mask used for measurements, where "n" is a normal mask and "w" is a more extensive line list to cover weak emission lines. (8) and (10) Redshift measurements for the 3880–5550 Å and CaT region based on the template fits and associated (1σ) error. A 10 km s^{-1} systematic error has been added due to wavelength calibration uncertainty. (9) and (11) Velocity dispersion measurements for the 3880–5550 Å and CaT region and associated (1σ) error.

(This table is available in its entirety in machine-readable form.)

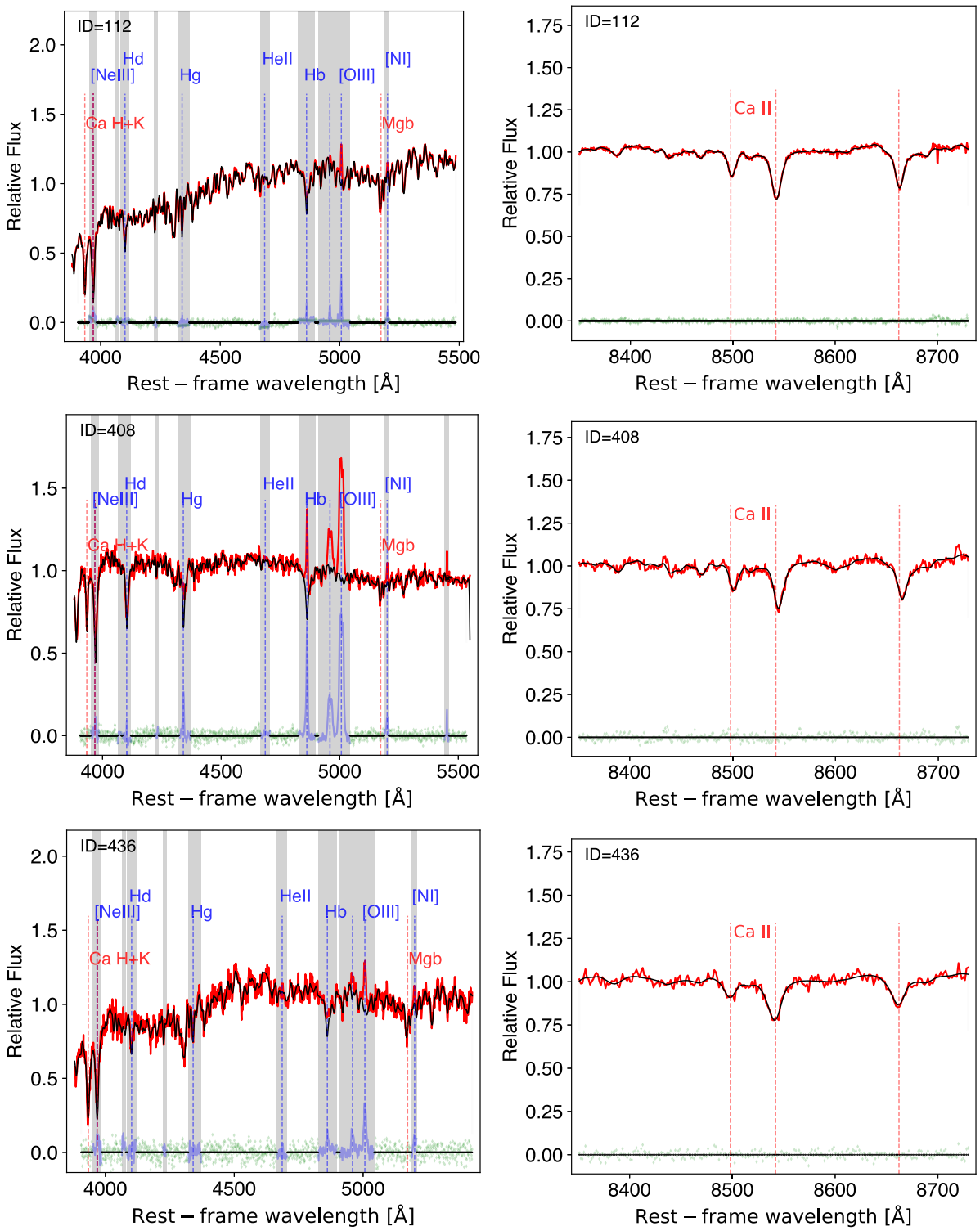

Figure 3. Examples of velocity dispersion fits for three AGN spectra (from top to bottom: BAT IDs 112, 408, and 436), representative of the three most common observational setups (from top to bottom: VLT/X-Shooter, SDSS, and Palomar/DBSP). The three spectra shown here illustrate the fitting quality typical of the top quartile, median, and bottom quartile of the velocity dispersion errors (from top to bottom: $\Delta\sigma_* = 4$, 7, and 11 km s^{-1}, respectively). In all panels, the red lines indicate the observed spectra, and the best-fitting templates are shown in black. The red dashed vertical lines indicate important absorption features, while the blue dashed vertical lines mark possible emission features that are masked out in the gray regions.

more than 80 km s^{-1}, while our sample has only ID = 548 2% (1/51), so the number of outliers is quite similar percentagewise.

A summary of the comparisons between different overlapping samples of σ_* measurements is provided in Table 3. In addition to the comparisons with the secondary spectra, within the best spectra, and with the literature, we also look at a subsample of the best spectra in the top three quartiles of the best measurements, with $\Delta\sigma_* < 11$ km s^{-1}, to better exclude unreliable outliers. In general, we do not find significant

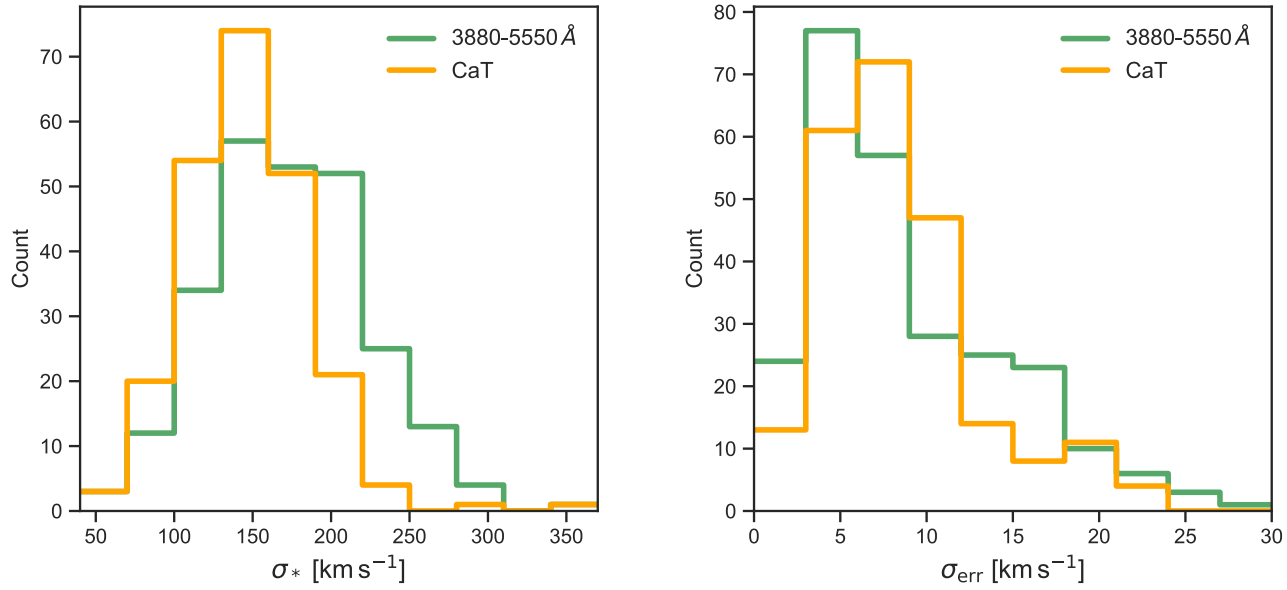

Figure 4. Distributions of velocity dispersions (left) and measurement errors (right) for the 3880–5550 Å ($N = 254$) and CaT ($N = 230$) fitting regions from the best fits. The median velocity dispersions from the 3880–5550 Å region are somewhat higher than those from the CaT region (173 and 144 km s^{-1}, respectively). This is due to the typically higher redshifts of the AGN for which a fit from the 3880–5550 Å region is available (median $z = 0.042$) compared to those with CaT measurements ($z = 0.024$), as the latter spectral region is limited by the increasing effect of telluric features (at $z > 0.065$).

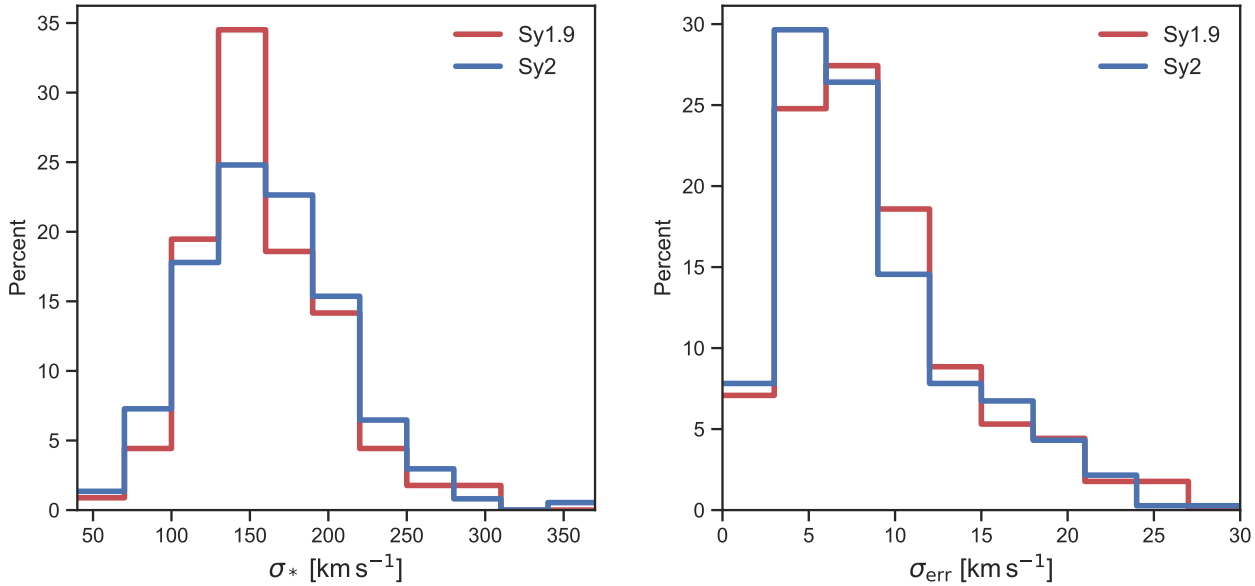

Figure 5. Distributions of velocity dispersions (left) and measurement errors (right) for Sy 1.9 ($N = 113$) and Sy 2 ($N = 371$). The two subsamples are very similar, with a median of 153 ± 5 and 157 ± 3 km s^{-1} for Sy 1.9 and Sy 2, respectively.

systematic offsets between samples, with the medians differing by at most 8 km s^{-1}, or <1 km s^{-1} when using the best spectra.

Given the large number of duplicate velocity dispersion measurements, it is possible to estimate the systematic scatter beyond the errors we report for each measurement to check whether the computed uncertainties are underestimated or overestimated. While there are several possible functional forms for the measurement error distribution and the intrinsic scatter in measurements of σ_*, past studies have generally found that the error distribution does not significantly change the scatter (see, e.g., Appendix B in Gultekin et al. 2009); we therefore prefer the Gaussian error distribution with Gaussian scatter, as it is straightforward. With this assumption, we have run a bootstrap simulation assuming the 1σ equivalent uncertainties of our σ_* measurements, provided by the `pPXF` (resampling) procedure, to generate a distribution of 1000 Gaussian errors within the two samples and estimated the corresponding rms and MAD. We then compared the simulated rms and MAD to the actual rms and MAD and found that the intrinsic scatter is larger than reported based on individual measurements. We can then subtract the simulated rms (or MAD) from the measured rms (or MAD) in quadrature to determine the additional intrinsic scatter. We find that our errors between samples are underestimated by 16–31 km s^{-1} in rms and 8–18 km s^{-1}. The underestimate in error scales with the predicted error, with the top three quartiles in the best spectra showing the smallest underestimates of the error at 14 km s^{-1} in rms and 8 km s^{-1} in MAD. This systematic

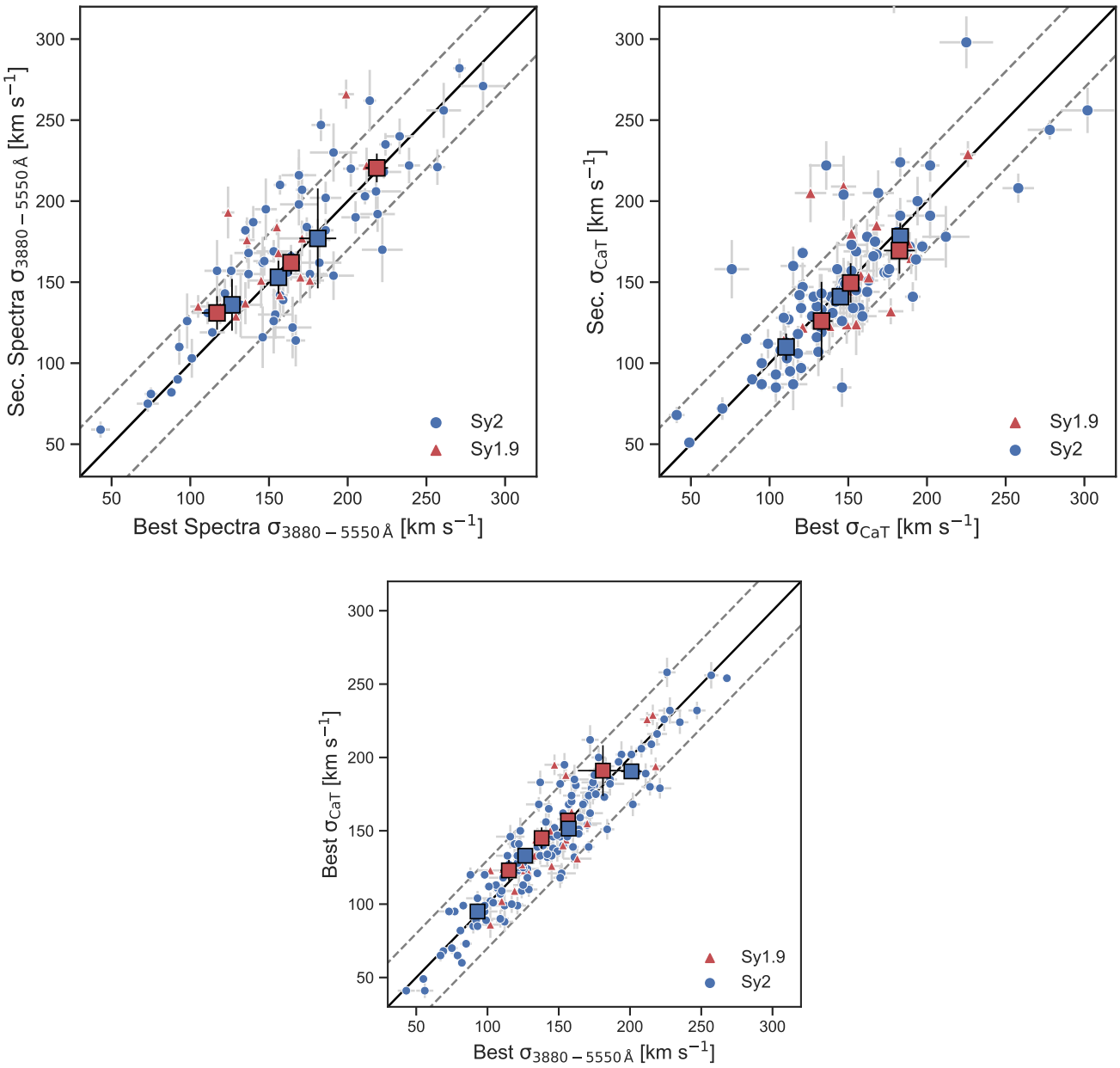

Figure 6. Top left: velocity dispersion measurements from the best spectra compared to lower-quality different secondary spectra in the blue region (3880–5550 Å). Here Sy 1.9 (with broad Hα) is shown by red triangles, and Sy 2 is shown by blue circles. Error bars (at 1σ) are shown in gray. A solid black line indicates the one-to-one relation with dashed gray lines indicating offsets of 30 km s^{-1}. The large squares indicate the binned medians for each subclass. Error bars on the plotted median values are equivalent to 1σ and calculated based on a bootstrap procedure with 100 realizations. The bin sizes were constructed to have equal numbers of sources in each bin. Top right: comparison between the velocity dispersion measurements from the best spectra and the secondary spectra in the CaT region (8350–8730 Å). Bottom right: comparison between the 3880–5550 Å and CaT within the single same best spectrum.

scatter is likely driven by a combination of several factors but is not, however, due to pPXF-based error estimation, as the comparisons include different observations, spectral regions, galaxy apertures, and spectral templates. However, we stress that, when making a comparison, it is important to consider this increased scatter (on the order of 8–18 or 16–31 km s^{-1} rms when considering outliers).

A further comparison with the σ_* measurements in BASS DR1 is provided in Appendix D.

4.2. Sample (In)completeness

The set of BASS DR2 AGN with σ_* measurements is completely free from biases related to inadequate instrumental resolution. This is thanks to our strategy of repeated targeting with higher spectral resolution setups in both the northern and southern hemispheres (with Palomar/DBSP in the north and VLT/X-Shooter or SOAR/Goodman in the south) providing an instrumental resolution of $\sigma_{\rm inst} = 19$–27 km s^{-1}. Still, about 9% of the Sy 1.9/Sy 2 sources in BASS DR2 (34/393) lack a stellar velocity dispersion measurement.[35] A complete list of the sources that lack a σ_* measurement is provided in Appendix E (Table 8). The main contribution to this (minor) incompleteness comes from AGN observed within the Galactic

[35] This excludes the 125 AGN in the bonus sample, drawn from the 105 month BAT catalog, where follow-up optical spectroscopy is ongoing.

Table 3
Velocity Dispersion Comparisons

S1	S2	N	$\langle\Delta\sigma_*\rangle$ (km s^{-1})	rms (km s^{-1})	rms Pred. (km s^{-1})	rms+ (km s^{-1})	Med. (km s^{-1})	MAD (km s^{-1})	MAD Pred. (km s^{-1})	MAD+ (km s^{-1})
(1)	(2)	(3)	(4)	(5)	(6)	(7)	(8)	(9)	(10)	(11)
3880–5550 best	3880–5550 secondary	78	−7.5	27.1	14.5	22.9	−6.0	19.5	8.0	17.8
CaT best	CaT secondary	101	−2.3	31.2	13.8	28.0	0.0	14.0	7.1	12.1
3880–5550 best	CaT best	266	−2.1	26.7	12.9	23.5	−0.5	13.5	6.1	12.1
3880–5550 best Q1–Q3	CaT best Q1–Q3	162	0.2	16.3	8.0	14.1	1.0	9.5	4.4	8.4
Composite best	Literature	51	−5.1	28.4	13.2	25.1	1.0	16.0	6.9	14.5

Note. The columns are as follows. (1) Primary measurement sample used from the best spectra for comparison; Q1–Q3 indicates the upper three quartiles in measurement error in the best spectra that also have a secondary measurement region. (2) Measurement sample used for comparison. (3) Number of measurements in each sample. (4) Mean offset between sample measurements. (5)–(7) The rms of the sample, predicted rms based on individual errors using bootstrapping, and additional rms based on subtraction of the predicted rms from the rms. (8) Median offset. (9)–(11) MAD of the sample, predicted MAD based on individual errors using bootstrapping, and additional MAD based on subtraction of the predicted MAD from the MAD.

plane, where high optical extinction makes high-quality spectroscopy and σ_* measurements more difficult.

Focusing on the subset of BASS DR2 sources that are seen outside the Galactic plane ($|b| > 10°$), the σ_* completion rate rises to 97% (326/335). Further focusing on $z < 0.1$ AGN, the completion rate is 99% (298/301), with only three AGN without high-quality measurements. For somewhat higher-redshift sources ($0.1 < z < 0.59$), the completion rate drops to 82% (28/34), driven by the limited S/N achievable within our longest exposures and the inability to use the CaT region due to telluric features. Among lower-redshift AGN outside the Galactic plane, the three obscured AGN without σ_* are largely mergers or emission line–dominated AGN. To demonstrate the challenges imposed by such systems, consider the dual AGN in Mrk 463E, which is completely dominated by emission lines with strong outflows (Treister et al. 2018).

4.3. BH Mass Estimates

A key goal of the BASS project is to generate a set of BH mass ($M_{\rm BH}$) measurements for the entire sample of BASS AGN. Only a small number of high-quality literature measurements from reverberation mapping, spatially resolved gas or stellar dynamics, and/or H_2O megamasers exist for the BASS AGN. As part of this study, we therefore provide estimates of the BH masses of the obscured AGN where velocity dispersion measurements can be used to estimate the BH mass following the well-established SMBH–host correlations.

For simplicity and consistency with the BASS DR1, we calculated $M_{\rm BH}$ using the best-fit $M_{\rm BH}-\sigma_*$ relation from Kormendy & Ho (2013):

$$\log(M_{\rm BH}/M_\odot) = 4.38 \times \log(\sigma_*/200\ {\rm km\ s^{-1}}) + 8.49. \quad (1)$$

The slope of this relation is consistent with that found by Gultekin et al. (2009), and both are considerably shallower than the slope of the relation derived by McConnell & Ma (2013), who reported a value of 5.64. The effect of using different scaling relations for $M_{\rm BH}$ is on the order of 0.1–0.3 dex at the median velocity dispersion (e.g., $\log(M_{\rm BH}/M_\odot) = 8$ versus $\log(M_{\rm BH}/M_\odot) =$ 7.7–7.9, $\sigma_* = 155$ km s^{-1}; McConnell & Ma 2013; Woo et al. 2013). The difference is somewhat larger at lower velocity dispersions (e.g., at 100 km s^{-1} $\log(M_{\rm BH}/M_\odot) = 7.2$ versus $\log(M_{\rm BH}/M_\odot) = 6.7$; McConnell & Ma 2013). Alternatively, using the more recent relations from Greene et al. (2020) for all galaxies including limits, the corresponding $M_{\rm BH}$ value is larger at 100 km s^{-1}, corresponding to $\log(M_{\rm BH}/M_\odot) = 7.5$.

We provide a full list of the resulting 484 $M_{\rm BH}$ estimates from the best σ_* measurements in Table 4. For those AGN where acceptable fits for both the 3880–5550 Å and CaT spectral regions are available, we also provide a weighted (mean) σ_* and corresponding weighted $M_{\rm BH}$ measurement. Using our large sample of measurements, we can understand how the real uncertainties on the σ_* measurements contribute to the error in inferring $M_{\rm BH}$. This is important because the highly nonlinear nature of the $M_{\rm BH}-\sigma_*$ scaling relation makes it difficult to simply add (in quadrature) the 8–18 km s^{-1} systematic error, as the same kilometer per second error will be much larger for low velocity dispersions.

We summarize several comparisons of inferred SMBH masses —between spectral regions, between best and secondary spectra, and to literature values—in Table 5. We find very small systematic offsets in the median ($\leqslant$0.07 dex) $M_{\rm BH}$ measured between different samples and somewhat larger offsets in the means due to outliers, though still $\leqslant$0.1 dex. In order to understand the scatter, we performed a simulation similar to the one done for velocity dispersions but using the lognormal distributions of $M_{\rm BH}$ and errors inferred from σ_* and associated errors. We used similar Gaussian distributions based on the 1σ errors to generate a grid of 1000 distributions within the two samples and estimated the rms and MAD. We find that there is additional scatter on the order of 0.2–0.4 dex in rms or 0.11–0.21 in MAD. We note that these are consistent with, and indeed somewhat smaller than, the intrinsic scatter around even the tightest observed $M_{\rm BH}-\sigma_*$ relations (e.g., Gultekin et al. 2009; Kormendy & Ho 2013).

To calculate AGN bolometric luminosities ($L_{\rm bol}$) and Eddington ratios ($\log L/L_{\rm Edd}$, $L/L_{\rm Edd}$), we follow the prescription used throughout the BASS DR2 (see Koss et al. 2022b). In brief, $L_{\rm bol}$ is calculated from the intrinsic luminosity in the 14–150 keV range, which is derived in Ricci et al. (2017; see their Table 12). This calculation was made using the 70 month average Swift/BAT 14–195 keV spectra plus data below 10 keV from Swift XRT, XMM-Newton, Chandra, Suzaku, and/or ASCA fit to detailed spectral models. We follow the prescription used in other BASS DR2 publications (Koss et al. 2022b) and use the 14–150 keV emission with a bolometric correction of 8, which is consistent with past studies (e.g., Vasudevan & Fabian 2009). The $L/L_{\rm Edd}$ is then calculated as $L/L_{\rm Edd} = L_{\rm bol}/(1.5 \times 10^{38}[M_{\rm BH}/M_\odot])$. More elaborate bolometric corrections are beyond the scope of the present work, as

Table 4
Best Velocity Dispersion and M_{BH} Measurements

BAT ID	Region	σ_* (km s^{-1})	log M_{BH} (log $M_\odot$)	σ_* Weighted (km s^{-1})	M_{BH} Weighted (log $M_\odot$)
(1)	(2)	(3)	(4)	(5)	(6)
1	3880–5550	126 ± 6	7.61 ± 0.09	125 ± 5	7.60 ± 0.07
4	3880–5550	146 ± 6	7.89 ± 0.07	123 ± 4	7.56 ± 0.06
7	3880–5550	205 ± 12	8.54 ± 0.11		
10	3880–5550	253 ± 14	8.94 ± 0.10		
13	CaT	131 ± 8	7.68 ± 0.12		
17	CaT	147 ± 7	7.90 ± 0.09		
20	3880–5550	294 ± 22	9.22 ± 0.14		
24	CaT	121 ± 7	7.54 ± 0.11	132 ± 6	7.7 ± 0.08
25	3880–5550	134 ± 6	7.73 ± 0.08	141 ± 6	7.83 ± 0.07
28	CaT	200 ± 3	8.49 ± 0.03		
29	CaT	135 ± 17	7.74 ± 0.23		
31	3880–5550	83 ± 1	6.82 ± 0.03	88 ± 1	6.94 ± 0.02
32	3880–5550	269 ± 29	9.05 ± 0.19		
33	CaT	82 ± 21	6.80 ± 0.44		
37	3880–5550	195 ± 10	8.45 ± 0.09	191 ± 8	8.41 ± 0.08
44	CaT	160 ± 7	8.06 ± 0.08		
49	CaT	190 ± 7	8.39 ± 0.07		
50	CaT	104 ± 5	7.24 ± 0.09	101 ± 4	7.18 ± 0.08
53	3880–5550	140 ± 5	7.82 ± 0.07	143 ± 4	7.85 ± 0.05
55	3880–5550	151 ± 9	7.96 ± 0.12	159 ± 8	8.06 ± 0.09
57	3880–5550	239 ± 7	8.83 ± 0.06	242 ± 6	8.85 ± 0.05
58	CaT	118 ± 5	7.49 ± 0.08		
62	CaT	131 ± 9	7.68 ± 0.13		
63	3880–5550	106 ± 1	7.29 ± 0.02	109 ± 1	7.33 ± 0.01
64	CaT	168 ± 5	8.16 ± 0.05	160 ± 4	8.07 ± 0.05
65	3880–5550	123 ± 16	7.56 ± 0.23		
70	CaT	121 ± 7	7.54 ± 0.11		

Note. The columns are as follows. (1) Catalog ID in the BAT survey (https://swift.gsfc.nasa.gov/results/bs70mon/). (2) Region having the lowest error in velocity dispersion measurement. (3) Best velocity dispersion measurement and associated (1σ) error. (4) Inferred M_{BH} based on σ_* using Kormendy & Ho (2013) M_{BH}–σ_* relation and associated error. (5) Weighted velocity dispersion as the average of the 3880–5550 Å and CaT dispersions, weighted by their respective error bars.

(This table is available in its entirety in machine-readable form.)

Table 5
M_{BH} Comparison Using Different σ_* Measurements

S1	S2	N	$\langle\Delta \log M_{BH}\rangle$	rms	rms Pred.	rms+	Med.	MAD	MAD Pred.	MAD+
3880–5550 best	3880–5550 secondary	78	−0.09	0.31	0.17	0.26	−0.07	0.23	0.09	0.21
CaT best	CaT secondary	101	−0.02	0.37	0.18	0.33	0.00	0.20	0.09	0.17
3880–5550 best	CaT best	266	−0.02	0.33	0.16	0.28	0.00	0.18	0.08	0.16
3880–5550 best Q1–Q3	CaT best Q1–Q3	162	0.01	0.23	0.11	0.20	0.01	0.13	0.06	0.11
Composite best	Literature	51	0.05	0.36	0.18	0.31	−0.02	0.22	0.09	0.20

Note. Column descriptions are the same as Table 3, unless otherwise noted. All M_{BH}-related quantities are listed in dex.

L_{bol} and L/L_{Edd} are used simply to illustrate the part of parameter space occupied by obscured BASS AGN.

The distributions of SMBH masses and Eddington ratios for the Sy 1.9 ($N = 113$) and Sy 2 ($N = 371$) sources in BASS are shown in Figure 8. The SMBH mass distributions for the two AGN subclasses are very similar, with medians of $\log(M_{BH}/M_\odot) = 8.01 \pm 0.05$ and 8.00 ± 0.03 for Sy 1.9 and Sy 2, respectively (standard deviations of 0.56 and 0.59 dex, respectively). A Kolmogorov–Smirnov (K-S) test indicates that the samples are not significantly different in their M_{BH} ($p = 0.45$). For Eddington ratios, the distributions are also very similar, with $\log L/L_{Edd} = -1.65 \pm 0.10$ and -1.72 ± 0.03 for Sy 1.9 and Sy 2, respectively (standard deviations of 0.77 and 0.64 dex, respectively). A K-S test indicates that the samples are not significantly different in their Eddington ratios ($p = 0.12$).

Figure 9 shows the distribution of our AGN in the σ_* (or M_{BH}) versus redshift parameter space. The lowest σ_* (and corresponding M_{BH}) that we could have measured, given our instrumental setups, is highlighted. Importantly, we also illustrate the limiting values of M_{BH} (and σ_*) corresponding to various values of L/L_{Edd}, given the BAT flux limit, to show the range of L/L_{Edd} that our study is sensitive to as a function of redshift. This figure is interesting for both the distribution of sources and the parameter space where sources are not detected. While BASS DR2 has the instrumental resolution to detect low-mass, super-Eddington SMBHs (i.e., $\lesssim 10^5\ M_\odot$), we do not find such systems despite having a "complete" sample of AGN, including obscured sources (perhaps missing only highly CT AGN, $N_H > 10^{25}$ cm^{-2}). Additionally, there is only a very small volume where the BAT survey detects SMBHs with extremely

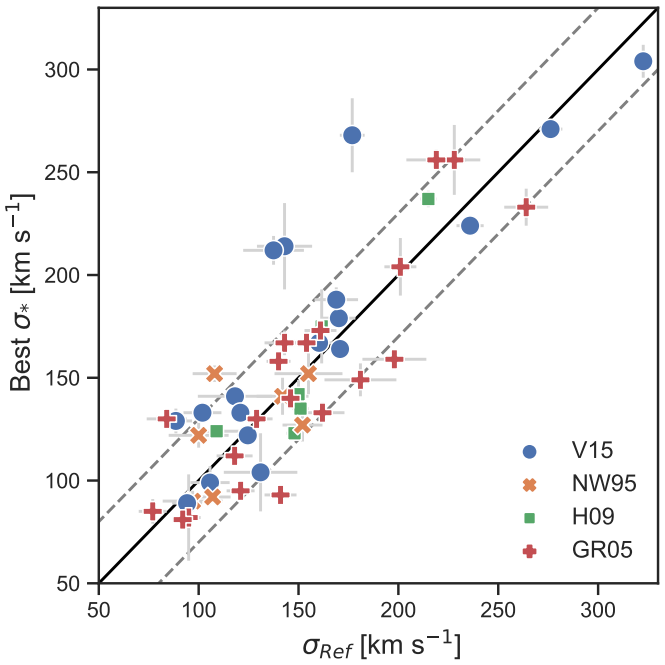

Figure 7. Comparison between the velocity dispersion measurements from the best spectra and the literature values for the same AGN. Error bars (at 1σ) are shown in gray. A black solid line indicates the one-to-one relation, with dashed gray lines indicating offsets of 30 km s^{-1}. The comparison samples are as follows: H09, Ho et al. (2009); GR05, Garcia-Rissmann et al. (2005); V15, van den Bosch et al. (2015); and NW95, Nelson & Whittle (1995).

low Eddington ratios, $\lesssim 10^{-5}$ (i.e., at $z < 0.007$). The detection of such objects would allow the study of the emission properties of advection-dominated accretion flows (Yuan & Narayan 2014). However, these radiatively inefficient accretion flows result in broadband spectral energy distributions that are thought to be markedly different from those characterizing standard, thin-disk accretion and are expected to be intrinsically fainter, making them even harder to detect with Swift/BAT (see, e.g., Ryan & MacFadyen 2017).

An elaborate investigation of the distributions of luminosities, BH masses, and Eddington ratios of all BASS DR2 AGN, relying in part on the σ_* measurements presented here and correcting for various selection effects that are present in the survey, is described in a companion paper (Ananna et al. 2022).

5. Discussion

As a nearly obscuration-free tracer of SMBH accretion up to CT levels, the 14–195 keV ultrahard X-rays surveyed by BAT/BASS provide a useful tracer of nearby obscured AGN activity over the whole sky. The >99% completeness of our spectroscopic coverage, combined with a very high spectral resolution ($\sigma_{\rm inst} \sim 25$ km s^{-1}) to effectively resolve even the narrowest absorption features for systems with small BHs, make it a unique legacy sample for future AGN studies, where a similar sensitivity, completeness, and/or resolution may be achievable. Here we review BASS in comparison to other AGN surveys, provide comparisons with direct measurements of SMBH masses, and investigate the feasibility of future programs of dynamical measurements and modeling to better measure the SMBH distribution of these AGN.

5.1. Comparison to Other Surveys

In Figure 10, we compare our BASS AGN σ_* measurements to those measured for spectroscopically selected star-forming galaxies (SFGs) and narrow-line AGN in the SDSS drawn from the OSSY catalog (Oh et al. 2011), all restricted to $z < 0.1$. The identification of (narrow-line) AGN and SFGs in SDSS is based on strong emission line ratio diagnostics (e.g., [O III] λ5007/Hβ vs. [N II] λ6583/Hα; Baldwin et al. 1981; Veilleux & Osterbrock 1987; Kewley et al. 2001). The majority of SFGs and a significant fraction of the AGN in the SDSS have σ_* that are below the nominal instrumental resolution of SDSS; thus, their true distribution below 70 km s^{-1} is highly uncertain. Nearly all of the BASS AGN have velocity dispersions that are larger than the average for SDSS-selected AGN (by $\sim$1.5×, i.e., 150 km s^{-1} versus 100 km s^{-1}). This is consistent with the fact that the SDSS narrow-line AGN population leans toward the more numerous, lower stellar mass galaxies compared to the BAT-selected AGN (see, e.g., Figure 12 in Koss et al. 2011a). Interestingly, the higher velocity dispersions of the BASS AGN (e.g., $\sim$150 km s^{-1}) are more consistent with the much more luminous type 2 quasars identified in the SDSS via strong emission line ratio diagnostics and luminous [O III] λ5007 emission at somewhat higher redshifts ($z \sim 0.3$, $\sim$160 km s^{-1}; Kong & Ho 2018).

One surprising result is that, despite the SFGs being roughly a factor of 220 more numerous in a similar redshift range and having low velocity dispersions ($\sigma_* \lesssim 70$ km s^{-1}) and thus potentially hosting lower-mass BHs, we do not detect their active counterparts within the Swift/BAT survey. If a significant population of super-Eddington low-$M_{\rm BH}$ AGN exists, they either lie below the flux limits of the BAT survey or are not hard X-ray sources. The $\sim$150 km s^{-1} is more consistent with SFGs at higher redshifts ($0.6 < z < 1$), such as those observed in COSMOS (Straatman et al. 2018).

Looking into the low-σ_*, low-mass end of the distribution for our BASS AGN in more detail, we note that our BASS DR2 sample has six low velocity dispersion AGN that have σ_* lower than the SDSS instrumental resolution of 70 km s^{-1}, which translates to BH masses $M_{\rm BH} \lesssim 10^{6.5}$ $M_\odot$ (see Equation (1)) that are also robustly measured through our highest spectral resolution setups ($\sigma_{\rm inst} \sim 25$ km s^{-1}, which translates to $10^{4.5}$ $M_\odot$). One of these six sources, NGC 7314, has been the focus of many X-ray variability studies (e.g., Emmanoulopoulos et al. 2016) motivated by the hope of identifying smaller SMBHs, suggested by the extremely low central stellar velocity dispersion. We finally compare our sources to some of the lowest-mass dwarf AGN selected from weak broad Hα line emission identified within the SDSS by Baldassare et al. (2020). As Figure 11 shows, our sources are typically located at lower redshifts ($z < 0.03$) and/or with higher σ_*. The small corresponding BH masses of the dwarf AGN, if detected above the BAT flux limit, would imply super-Eddington accretion, which may not necessarily be detected in the BAT band.

Considering the high-σ_*, high-mass end of the (active) galaxy population, in Figure 12, we compare the BASS AGN σ_* distribution to that of the HETMGS. The HETMGS survey was designed to find nearby galaxies where the SMBH sphere of influence (SOI) can be resolved by seeing-limited spectroscopy. This selection scheme means HETMGS includes some small but nearby galaxies that appear sufficiently large on the

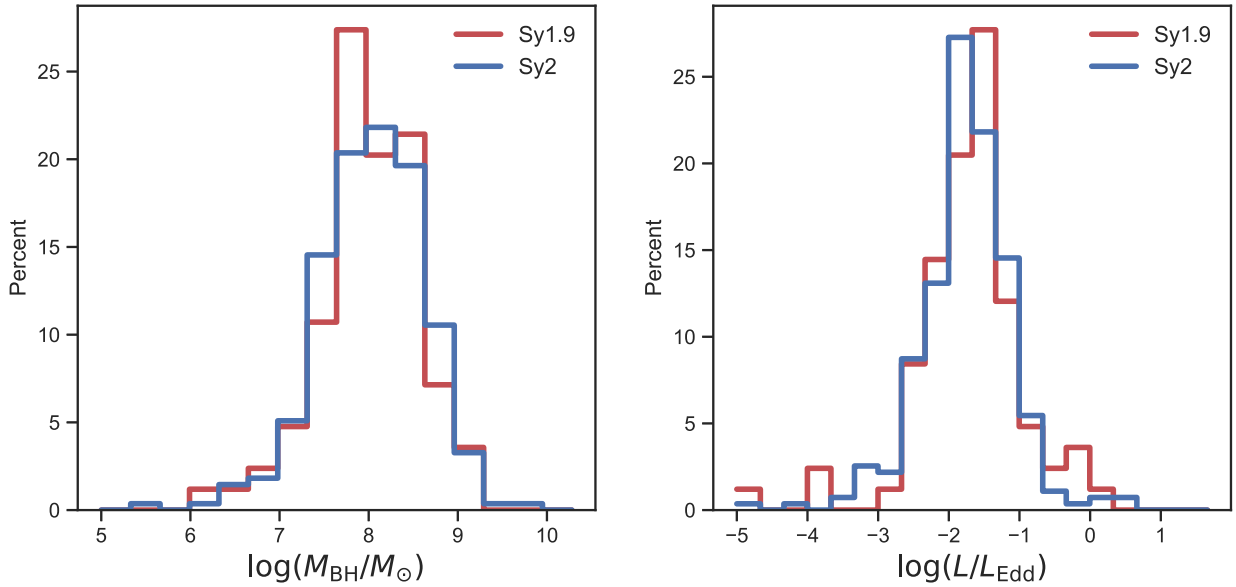

Figure 8. Frequency distributions of SMBH masses and Eddington ratios for Sy 1.9 ($N = 113$) and Sy 2 ($N = 371$).

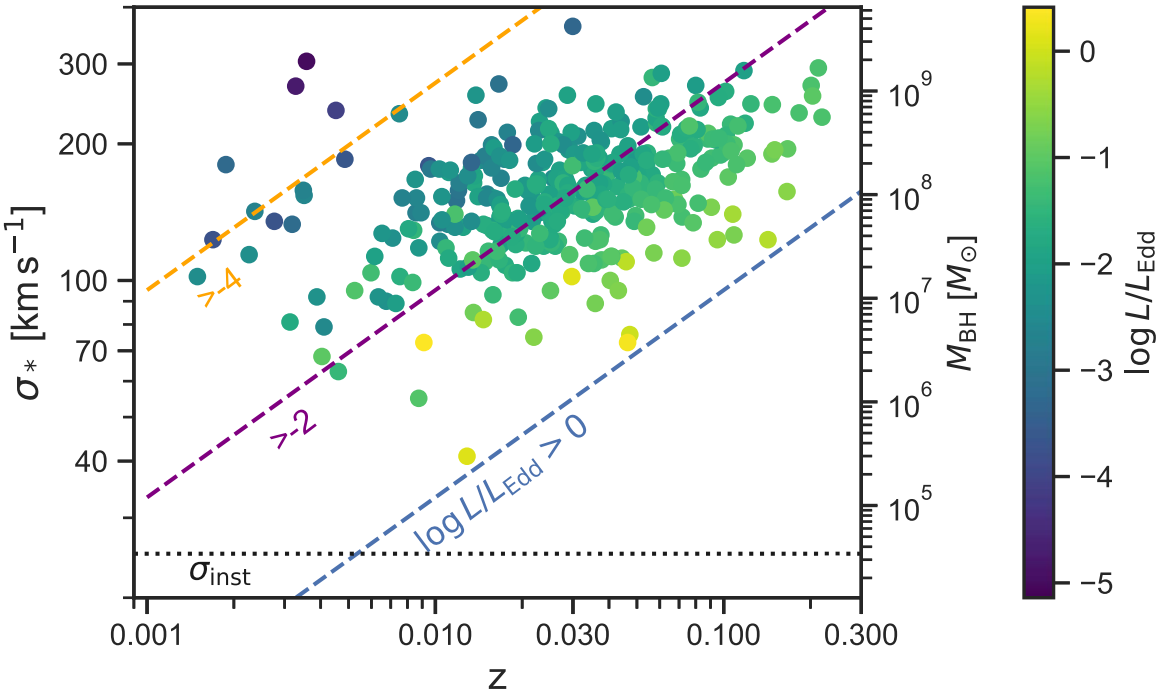

Figure 9. Plot of the distribution of σ_* and M_{BH} (based on the Kormendy & Ho 2013 relation) with redshift. The color bar indicates the Eddington ratio (L/L_{Edd}) of the AGN. Error bars in σ_* span 1–29 km s^{-1}, with a median of 7 km s^{-1}. The effective sensitivity limits on the Eddington ratio due to the survey flux limits are illustrated with diagonal dashed lines. For instance, the flux limit at $z = 0.01$ ($L_{bol} = 1.8 \times 10^{43}$ erg s^{-1}) corresponds to an $L/L_{Edd} = 1$ (blue dashed line) source with $M_{BH} = 1.5 \times 10^5\ M_\odot$ or $\sigma_* = 35$ km s^{-1}. Therefore, any sources detected at $z = 0.01$ with $\sigma_* < 35$ km s^{-1} will always be super-Eddington because of the survey flux limits. The black dotted line indicates the instrumental limits of the survey for velocity dispersion measurements. One higher-redshift AGN, BAT ID = 1204 ($\sigma_* = 364$ km s^{-1}, Eddington ratio = 0.20, $z = 0.597$), is not shown.

sky (i.e., due to their small distance). We limit our comparison between HETMGS and BASS AGN to $0.02 < z < 0.04$, adopting $z > 0.02$ to focus only on the most massive galaxies and $z < 0.04$ because the HETMGS survey does not extend further than this. Interestingly, the typical velocity dispersions in the HETMGS (sub)sample are significantly larger than those of the BASS AGN (mean values of ∼275 versus ∼150 km s^{-1}, respectively). This highlights the fact that the BASS AGN are not hosted in the largest bulges known in the nearby universe, which are predominantly in passive galaxies, but rather in an intermediate population with likely lower masses. Combining the largest velocity dispersions observed within HETMGS of ≈400 km s^{-1} and the BAT survey flux limit (see Figure 9), we conclude that BASS is not sensitive enough to detect SMBHs accreting at extremely low rates, $L/L_{Edd} \lesssim 10^{-5}$, and hence probe the advection-dominated regime of SMBH accretion.

In summary, the BASS AGN tend to avoid both the highest- and lowest-mass systems, as well as ones with super-Eddington accretion, and the selection function is complicated. For a deeper understanding of the intrinsic M_{BH} and L/L_{Edd}

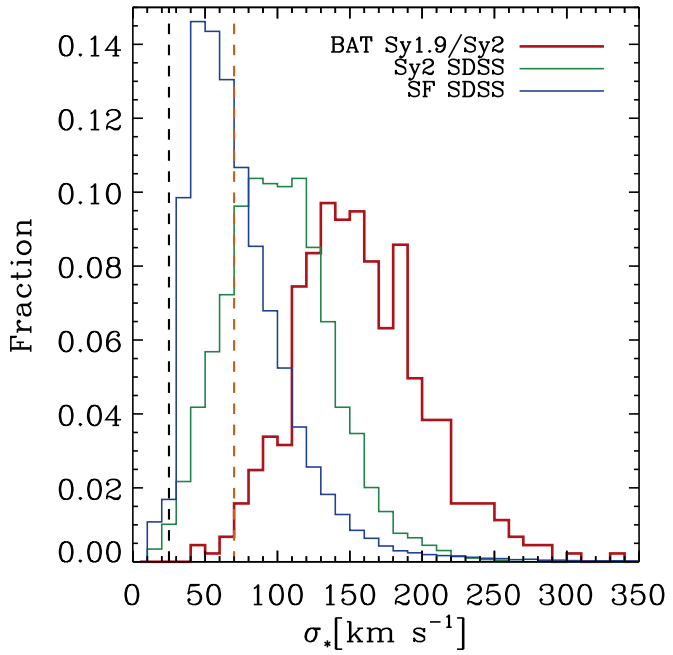

Figure 10. Comparison of nearby obscured BASS AGN (Sy 1.9 and Sy 2, $z < 0.1$, $N = 444$) to optically selected nearby ($z < 0.1$) narrow-line Seyferts ($N = 4926$) and SFGs ($N = 97{,}216$) in the SDSS DR7 from the OSSY catalog (Oh et al. 2011). The orange dashed line indicates the instrumental limit of the SDSS (∼70 km s^{-1}) compared to the instrumental limits for BASS AGN, shown with a black dashed line (∼25 km s^{-1}).

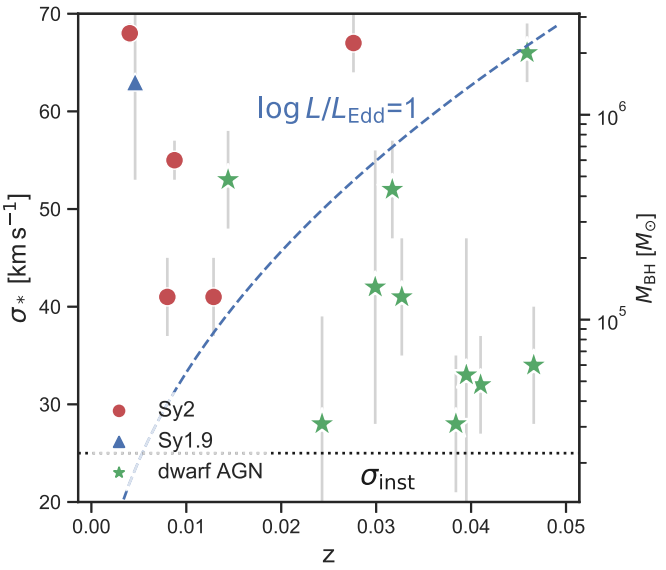

Figure 11. Comparison of the BASS AGN to the velocity dispersion of dwarf galaxies hosting AGN (Baldassare et al. 2020). This dwarf AGN sample was identified in the SDSS at $z < 0.055$ based on emission line diagnostics and broad lines in Hα (Reines et al. 2013). The dashed blue line indicates the sky sensitivity limit for a source at the Eddington limit ($L/L_{\rm Edd} = 1$) at the BAT survey all-sky flux limits, so any Sy 1.9 and Sy 2 detected by BAT below this line would be super-Eddington. The black dotted line indicates the BASS instrumental limits for velocity dispersion measurements ($\sigma_{\rm inst} \sim 25$ km s^{-1}), which is the similar to the the Keck study ($\sigma_{\rm inst} = 23$ km s^{-1}).

distributions, we again refer to the companion dedicated study by Ananna et al. (2022).

5.2. Comparison with Higher-precision Direct Measurements

The velocity dispersion measurements studied here provide a useful proxy to $M_{\rm BH}$ for large statistical studies of obscured AGN. However, direct measurements provide much higher accuracy and naturally avoid the usage of empirical scaling relations. For obscured AGN, the relevant direct $M_{\rm BH}$ measurement methods include dynamical gas and/or stellar modeling (e.g., Kormendy & Ho 2013) and H_2O megamasers (e.g., Staveley-Smith et al. 1992). A list of 64 direct measurements for the 70 month BAT AGN was compiled as part of the BASS DR1 (Koss et al. 2017) and more recently for the DR2 (Koss et al. 2022b), though the majority of masses in these lists were derived from reverberation mapping campaigns of unobscured (broad-line) AGN (e.g., Bentz et al. 2009), which are not part of the present sample of host-dominated, narrow-line AGN. The updated DR2 list in Koss et al. (2022b) matches the BASS AGN to compilations of megamaser measurements (e.g., Kuo et al. 2011) and the latest large samples of direct measurements of early- and late-type spiral galaxies (e.g., 145 galaxies in Sahu et al. 2019a). Despite the BASS AGN being the brightest X-ray-selected AGN across the sky, there are only 18 of these measurements, including 10 megamasers, four dynamical gas measurements, and four stellar dynamical measurements that overlap with our velocity dispersion sample. The BAT-detected AGN at the center of the Perseus cluster (Perseus A; aka NGC 1275) also does not have a successful σ_* measurement due to the strong emission lines present in the spectrum. This source does have a dynamical (molecular) gas measurement reported by Scharwachter et al. (2013), although that paper cautions that the gas mass in the core may be nonnegligible; thus, their measurement could be considered as an upper limit.

In Figure 13, we compare the available direct $M_{\rm BH}$ measurements to those derived here through our σ_* measurements and the $M_{\rm BH}$–σ_* relation. There are clearly large discrepancies among megamasers, where the σ_*-based estimates seem to significantly overpredict the $M_{\rm BH}$ (median offset of 0.7 dex). In contrast, our σ_*-based measurements show better agreement with stellar and/or gas dynamical measurements, although the latter are only available for a small sample. These findings are consistent with studies of much larger samples of spiral and early-type galaxies, which have found that spiral galaxies with nonmaser dynamical $M_{\rm BH}$ measurements do not appear to show an offset, but megamasers are significantly offset (e.g., 0.6 ± 0.14 dex; Greene et al. 2016). It is still unclear whether this offset in megamasers is because they trace the true $M_{\rm BH}$ distribution, while the nonmaser $M_{\rm BH}$ population is biased because of the inability to resolve the SOI of small SMBHs ($<10^7\ M_\odot$). Or the maser population maybe somewhat offset because of a stronger rotational contribution to the stellar velocity dispersion (e.g., Caglar et al. 2020). Alternatively, the nonmaser distribution could be the true one. We leave further discussion to works with much larger samples of direct measurements, where these differences can be addressed in a much more comprehensive way.

5.3. Feasibility of Additional Direct Measurements

Given the extremely small sample of high-quality megamaser and dynamical measurements (i.e., only 3.7%, or 18/484 AGN) and large offsets compared to the few megamaser measurements, it is worth considering how many more AGN-dominated galaxy centers could potentially be spatially resolved to yield BH masses derived from dynamical modeling of gas and/or stars. For these studies, facilities such as NIR

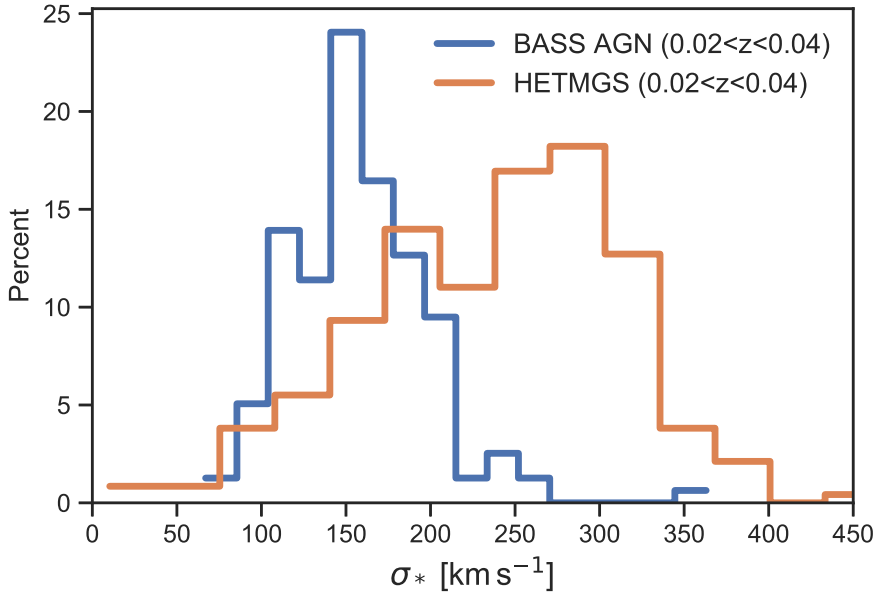

Figure 12. Comparison of the BASS AGN to the velocity dispersions of the HETMGS survey (van den Bosch et al. 2015), which was designed to select the most massive BHs (and highest velocity dispersions) at all redshifts that could be dynamically resolved. For both samples, the redshift range is limited to $0.02 < z < 0.04$ to avoid the low-mass galaxies at low redshifts in HETMGS that can be resolved.

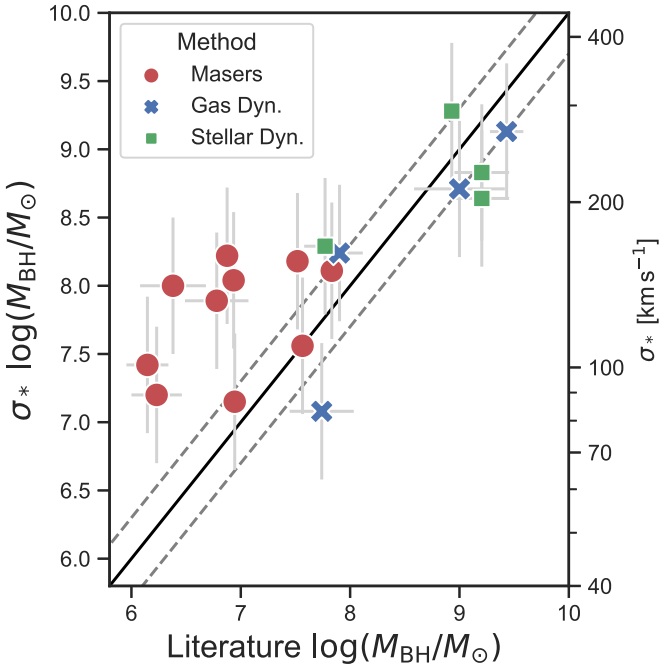

Figure 13. Comparison of the inferred $M_{\rm BH}$ mass estimate from σ_* compared to direct measurements using megamaser compilations (Greene et al. 2016), as well as stellar (Neumayer 2010; Medling et al. 2011; Walsh et al. 2012) and gas dynamics (Tadhunter et al. 2003; Capetti et al. 2005; Wold et al. 2006) measurements. Error bars in $M_{\rm BH}$ inferred from σ_* have been set to 0.5 dex based on past comparisons with direct measurements (e.g., 0.44 dex; Gultekin et al. 2009).

integral field units, assisted by adaptive optics (AO; e.g., VLT/MUSE or Keck/OSIRIS) or submillimeter interferometers (e.g., ALMA or NOEMA), could be considered.

In these dynamical models, to detect the influence of the BH, the region within which the BH gravity dominates over that of the host must be spatially resolved. The size of this region, referred to as the SOI, is commonly given by $r_{\rm SOI} = GM_{\rm BH}\sigma_*^{-2}$. Given a distance, D, the apparent size projected on the sky is $\theta_{\rm SOI} = r_{\rm SOI} D^{-1}$. This simple prescription is derived assuming virialized, spherically symmetric, and isotropic gas motion in the target galaxy nucleus (see, e.g., van den Bosch et al. 2015). Plugging in our $M_{\rm BH}$–σ_* relation (see Equation (1)) and rescaling to a size in parsecs results in

$$r_{\rm SOI} = 33\ {\rm pc}\left(\frac{\sigma_*}{200\ {\rm km\ s^{-1}}}\right)^{2.38}. \quad (2)$$

As an example, an SMBH with $M_{\rm BH} = 10^8\ M_\odot$ (or $\sigma_* = 155$ km s^{-1}) would have $r_{\rm SOI} = 18$ pc, and at the median redshift of the BASS AGN ($z = 0.03$), it would have $\theta_{\rm SOI} = 0\farcs03$.

We use this definition to determine whether resolving the SOI is feasible for any given galaxy. There can be significant additional challenges to obtaining measurements for dynamical modeling (e.g., stellar mass-to-light ratios and/or nonaxisymmetric structures). This is combined with instrumental and observational challenges, such as the requirement of AO instruments to have a bright nearby tip-tilt star and the limited spectral range in the K band ($\sim$2 μm) for CO-bandhead observations of redshifted sources. Given all of these challenges, our following attempt to illustrate potential sources for follow-up observations should be considered as a first step to identify initial candidates.

The calculated $r_{\rm SOI}$ (in parsecs) for our sample of BASS AGN with quality σ_* measurements are shown in Figure 14. Clearly, there is a large number of candidate AGN that could possibly be resolved using direct measurements. Existing facilities could resolve the stellar dynamics in 128/484 of our sources (27%, or $128 - 17 = 111$ where such measurements do not yet exist). For gas dynamics, the picture may be even more positive, given the higher resolution that can be achieved with submillimeter interferometers. Specifically, a resolution of $0\farcs03$, achievable with ALMA over much of the sky (e.g., $\delta < 25°$), could potentially provide direct $M_{\rm BH}$ measurements for 325/484 of our obscured AGN (68%, or $325 - 18 = 307$ with no prior measurements). We note that gas dynamical measurements require Keplerian motions for a relatively large reservoir of circumnuclear gas, as well as high-resolution optical imaging (with the Hubble Space Telescope; FWHM $= 0\farcs08$) to estimate

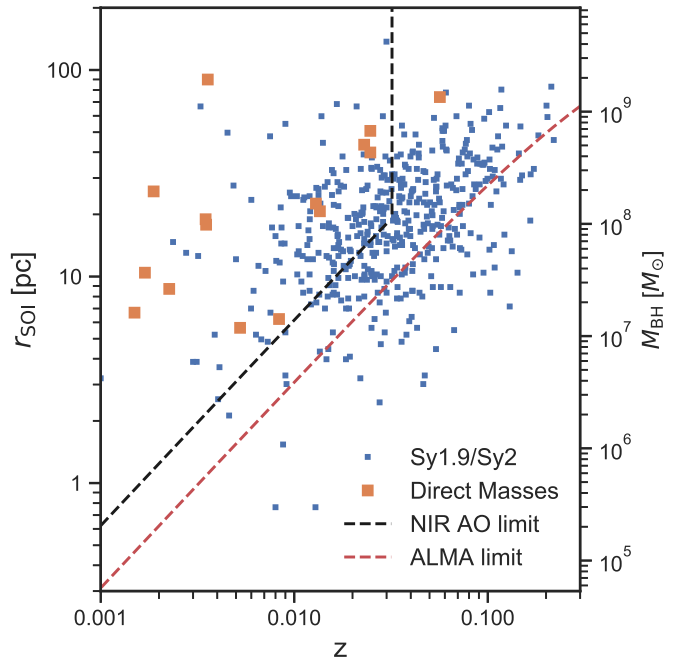

Figure 14. Estimated SOI (r_{SOI}) in parsecs for obscured AGN in this sample based on the velocity dispersion measurements. The dashed lines indicate the ability to detect the dynamical influence of the SMBH, assuming the observations have a minimum spatial resolution of twice the r_{SOI} (Davis 2014). The black dashed lines indicate the limiting resolution for AO observations of stellar dynamics using the CO bandheads in the K band, assuming a good tip-tilt star is available (0.″06 FWHM). The vertical line is due to these bands shifting out of the K band (at $z = 0.032$). The red dashed line indicates the capabilities of ALMA to resolve the gas dynamics for the CO 2–1 line at higher spatial resolutions (0.″03 FWHM). The large orange squares indicate sources with dynamical and/or megamaser measurements.

the contribution of stellar mass in the region near the SMBH. However, the most recent of these gas dynamical measurements have been done at similar spatial scales (e.g., $\theta_{SOI} = 0.''07$; Smith et al. 2021) and with gas detections in the inner regions of similarly small regions near the SMBH (e.g., $r_{SOI} = 13$ pc; Davis et al. 2017). The best available ALMA resolution will also increase again in late 2022, thanks to the high-frequency, long-baseline capabilities in the highest bands (e.g., $\sim 0.''01$).

Increasing the sample size in M_{BH}–σ_* to better understand the relation is a critical goal within BASS, as it is sensitive to the strongest accreting SMBHs in the nearby universe, where there may be more gas available for direct imaging measurements. A number of these ALMA programs to enlarge the sample of high spatial resolution observations among BASS AGN are just beginning or already ongoing. For gas dynamical measurements, an ALMA program to obtain CO(2–1) measurements at ≈100 pc resolution for 33 nearby and luminous AGN was recently completed, with additional programs ongoing, and generally, more than 100 BASS AGN now have ALMA observations at CO(2–1) regardless of resolution. Additionally, single-dish observations to measure whether the AGN lie in galaxies that are sufficiently gas-rich to facilitate high-resolution molecular gas observations have been carried out with APEX (Koss et al. 2021) for 213 nearby AGN ($0.01 < z < 0.05$), although naturally higher resolutions will be needed to confirm the presence of sufficient gas in the inner regions of these galaxies.

6. Summary

We present new measurements of central stellar velocity dispersions for 484 Sy 1.9 and Sy 2 luminous AGN drawn from the BASS DR2. We have developed a set of high-resolution spectral templates ($R = 10{,}000$) from the VLT/X-Shooter library to take advantage of the very high spectral resolutions of many of the spectra we used ($R \simeq 5000$, $\sigma_{inst} = 25$ km s^{-1}). This constitutes the largest study of X-ray-selected obscured AGN with velocity dispersion measurements and includes 956 independent measurements of the spectral regions relevant for the Ca II H and K λ3969, 3934 and Mg I λ5175 (3880–5550 Å) and CaT (8350–8730 Å) absorption features from 642 spectra. Our measurements span a wide range, $\sigma_* = 40$–360 km s^{-1}, corresponding to 4–5 orders of magnitude in SMBH mass ($M_{BH} \sim 10^{5.5-9.6}\ M_\odot$). Combined with the wide range in bolometric luminosity probed by the BAT all-sky survey ($L_{bol} \sim 10^{42-46}$ erg s^{-1}), we can explore an unprecedentedly broad range in Eddington ratios, $L/L_{Edd} \sim 10^{-5}$ to 2. Thus, this BASS DR2 Sy 1.9/Sy 2 sample represents a significant advance with a nearly complete census of velocity dispersions of hard X-ray–selected obscured AGN in the local universe ($z < 0.2$), covering 99% of nearby AGN ($z < 0.1$) and 82% at higher redshifts ($0.1 < z < 0.6$; outside the Galactic plane).

Using this large survey of central stellar velocity dispersions, we draw the following insights.

1. With a sample of 956 velocity dispersion measurements with significant duplications and two spectral regions (3880–5550 and CaT), we find that there is no significant offset between the two regions. However, there is a larger intrinsic scatter than expected (e.g., 8–18 km s^{-1} MAD) based on fitting errors due to the presence of outliers (e.g., 14–28 km s^{-1} rms). This leads to additional uncertainties in the scatter of the inferred SMBH measurements of 0.11–0.21 dex in MAD or 0.2–0.4 dex in rms.
2. The obscured BASS AGN occupy a unique space with their velocity dispersion properties, having much higher velocity dispersions (i.e., 150 versus 100 km s^{-1}) than the more numerous, optically selected narrow-line AGN (i.e., drawn from the SDSS) but not having a significant population of the highest velocity dispersions (i.e., >250 km s^{-1}) of the nearby universe.
3. Despite having sufficient spectral resolution to resolve very small BHs, we do not find a significant population of low-redshift, low-M_{BH} ($\lesssim 10^6\ M_\odot$), super-Eddington sources among BAT ultrahard X-ray–selected AGN.
4. Based on preliminary estimates of the SOI for the SMBHs in our sample, existing facilities can obtain direct M_{BH} measurements using stellar and gas dynamics for a considerably larger number of AGN than what is currently available.

To summarize, the BASS DR2 catalog of stellar velocity dispersion measurements and the implied BH masses provide an extremely useful resource for studies of the low-redshift population of actively accreting SMBHs and their host galaxies.

We thank Vivian Baldassare and Amy Reines for their assistance with dwarf AGN masses. We acknowledge support from NASA through ADAP award NNH16CT03C (M.K.); the Israel Science Foundation through grant No. 1849/19 (B.T.);

the European Research Council (ERC) under the European Union's Horizon 2020 research and innovation program through grant agreement No. 950533 (B.T.); FONDECYT Regular 1190818 (E.T., F.E.B.) and 1200495 (E.T., F.E.B); FONDECYT Postdoctoral Fellowship 3210157 (A.R.); ANID grants CATA-Basal AFB-170002 (E.T., F.E.B.), ACE210002 (E.T., F.E.B.), and FB210003 (C.R., E.T., F.E.B.); ANID Anillo ACT172033 and Millennium Nucleus NCN19_058 (E. T.); Millennium Science Initiative Program ICN12_009 (F.E. B.); an ESO fellowship (M.H., J.M.); Fondecyt Iniciacion grant 11190831 (C.R.); the National Research Foundation of Korea grant NRF-2020R1C1C1005462 and the Japan Society for the Promotion of Science ID 17321 (K.O.); Comunidad de Madrid through the Atracción de Talento Investigador Grant 2018-T1/TIC-11035 (I.L.); YCAA Prize Postdoctoral Fellowship (M. B.); Conselho Nacional de Desenvolvimento Científico e Tecnológico (CNPq; Proj. 311223/2020-6, 304927/2017-1, and 400352/2016-8); Fundação de amparo à pesquisa do Rio Grande do Sul (FAPERGS; Proj. 16/2551-0000251-7 and 19/1750-2); and Coordenação de Aperfeiçoamento de Pessoal de Nível Superior (CAPES; Proj. 0001; R.R.). This work was performed in part at the Aspen Center for Physics, which is supported by National Science Foundation grant PHY-1607611. We acknowledge the work done by the Swift/BAT team and the 50+ BASS scientists to make this project possible.

Some of the optical spectra were taken with DoubleSpec at Palomar via Yale (PI: M. Powell; 2017-2019, 16 nights), as well as Caltech (PI: F. Harrison) and JPL (PI: D. Stern) from programs from 2013–2021.

This work made use of observations collected at the European Southern Observatory under ESO programs 0101.A-0765(A), 0101.B-0456(B), 0102.A-0433(A), 0102.B-0048, 0103.A-0521(A), 0103.A-0777(A), 0104.A-0353(A), 090.A-0830(A), 092.B-0083(A), 093.A-0766(A), 095.B-0059(A), 098.A-0635(B), 099.A-0403(A), 099.A-0403(B), 094.B-0321(A), 098.B-0551(A), 60.A-9421(A), and 60.A-9100(J). Based on observations from six CNTAC programs: CN2018A-104, CN2018B-83, CN2019A-70, CN2019B-77, CN2020A-90, and CN2020B-48 (PI: C. Ricci). Based on NOIRLab proposals (2012A-0463; PI: M. Trippe). Based on observations obtained at the Southern Astrophysical Research (SOAR) telescope, which is a joint project of the Ministério da Ciência, Tecnologia e Inovações (MCTI/LNA) do Brasil, the US National Science Foundation's NOIRLab, the University of North Carolina at Chapel Hill (UNC), and Michigan State University (MSU).

Some of the data presented herein were obtained at the W. M. Keck Observatory, which is operated as a scientific partnership among the California Institute of Technology, the University of California, and the National Aeronautics and Space Administration. The Observatory was made possible by the generous financial support of the W. M. Keck Foundation. The authors wish to recognize and acknowledge the very significant cultural role and reverence that the summit of Maunakea has always had within the indigenous Hawaiian community. We are most fortunate to have the opportunity to conduct observations from this mountain.

This research has made use of NASA's ADS Service. This research has made use of the NASA/IPAC Infrared Science Archive, which is operated by the Jet Propulsion Laboratory, California Institute of Technology, under contract with the National Aeronautics and Space Administration.

Funding for SDSS-III has been provided by the Alfred P. Sloan Foundation, the Participating Institutions, the National Science Foundation, and the U.S. Department of Energy Office of Science. The SDSS-III website is http://www.sdss3.org/. The SDSS-III is managed by the Astrophysical Research Consortium for the Participating Institutions of the SDSS-III Collaboration, including the University of Arizona, the Brazilian Participation Group, Brookhaven National Laboratory, Carnegie Mellon University, the University of Florida, the French Participation Group, the German Participation Group, Harvard University, the Instituto de Astrofisica de Canarias, the Michigan State/Notre Dame/JINA Participation Group, Johns Hopkins University, Lawrence Berkeley National Laboratory, the Max Planck Institute for Astrophysics, the Max Planck Institute for Extraterrestrial Physics, New Mexico State University, New York University, Ohio State University, Pennsylvania State University, the University of Portsmouth, Princeton University, the Spanish Participation Group, the University of Tokyo, the University of Utah, Vanderbilt University, the University of Virginia, the University of Washington, and Yale University.

Facilities: IRSA, Keck:I (LRIS), Magellan:Clay, Hale (Doublespec), Swift (BAT), VLT:Kueyen (X-Shooter), VLT:Antu (FORS2), SOAR (Goodman)

Software: astropy (Astropy Collaboration et al. 2013), Matplotlib (Hunter 2007), Numpy (van der Walt et al. 2011).

Appendix A
Emission Lines Masked

A list of the masked emission lines is given in Table 6.

Table 6
Emission Lines Masked in `pPXF` Host Galaxy Fitting

Emission Line	Wavelength (Å)
H8 + He I	3889.1
[Ne III]	3967.41
[S II]	4071.24
Hδ	4101.76
[Fe V]	4229
Hγ	4340.47
[O III]	4363.21
He II	4686
Hβ	4861.33
[O III]	4958.92
[O III]	5006.84
[N I]	5200
Mask for Weaker Lines	
He I	4026
[Ar IV]	4712
[Ar IV]	4740
[Fe VI]	5146
[Fe VII]	5159
[Fe VIII]	5176
[Ca V]	5309
[Fe VI]	5485
[Cl III]	5518
[Cl III]	5538
O I	8446
[Cl II]	8578.7
[Fe II]	8617
Pa 12	8750
Pa 11	8863

Appendix B
Excluded Templates from Hierarchical Clustering

Examples of excluded templates from clustering are provided in Figure 15.

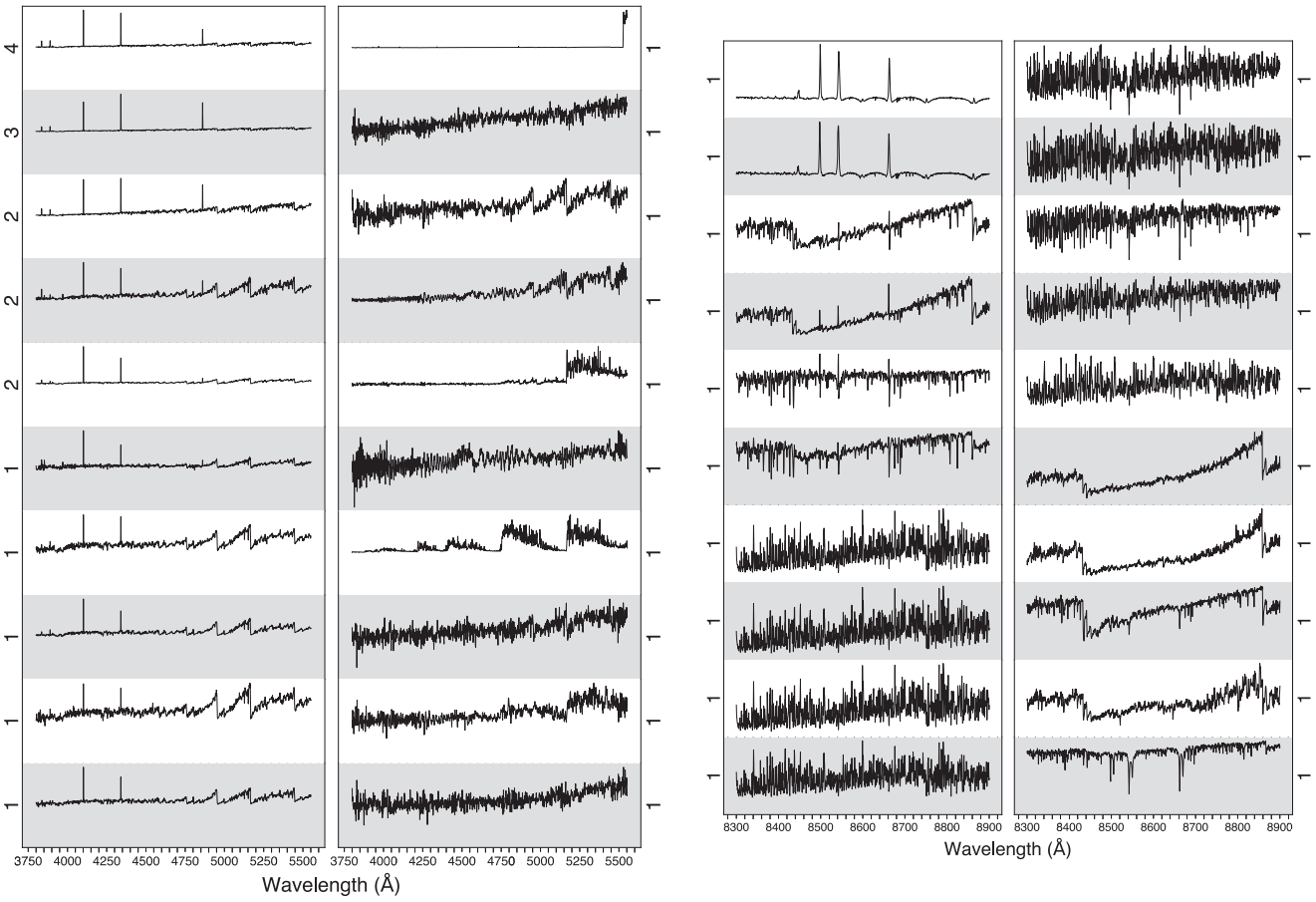

Figure 15. Examples of excluded X-Shooter templates from the hierarchical clustering analysis. Left: UVB templates that were excluded due to emission line features. Left middle: UVB templates that were excluded because of low S/N or because they were only found in one spectrum. The numbers on the left and right sides of the figure indicate the number of spectra the features were found in in the clustering analysis. Right middle and right: Examples of excluded X-Shooter VIS templates from hierarchical clustering analysis.

Appendix C
Secondary Velocity Dispersion Measurements

Here we provide secondary measurements in Table 7.

Table 7
Secondary Spectral Measurements

BAT ID	Galaxy	DR2 Type	Tele./Inst.	Res. Blue (Å)	Res. Red (Å)	Mask	$z_{3880-5550\ Å}$ (km s^{-1})	$\sigma_{3880-5550\ Å}$ (km s^{-1})	z_{CaT} (km s^{-1})	σ_{CaT} (km s^{-1})
13	LEDA 136991	Sy 2	Palomar/DBSP	4.1	4.9	n			3827 ± 11	107 ± 15
17	ESO 112-6	Sy 2	VLT/X-Shooter	1.3	1.4	n			8897 ± 10	150 ± 13
28	NGC 235A	Sy 1.9	Gemini/GMOS	4.8	⋯	n	6869 ± 5	188 ± 6		
50	ESO 243-26	Sy 2	SOAR/GMAN	2.7	⋯	w			5968 ± 4	85 ± 6
53	UM 85	Sy 2	Palomar/DBSP	4.1	4.9	w	12,536 ± 10	187 ± 10	12,516 ± 11	145 ± 15
57	3C 33	Sy 2	Palomar/DBSP	2.3	1.8	n	18,302 ± 14	222 ± 11		
63	NGC 454E	Sy 2	SOAR/GMAN	2.7	⋯	w			3730 ± 2	95 ± 3
70	MCG+8-3-18	Sy 2	Palomar/DBSP	4.8	6.5	w			6351 ± 10	147 ± 15
72	NGC 526A	Sy 1.9	SOAR/GMAN	2.7	⋯	w			5789 ± 4	153 ± 4
81	ESO 244-30	Sy 2	SOAR/GMAN	2.7	⋯	w			7878 ± 6	100 ± 6
83	ESO 353-9	Sy 2	SOAR/GMAN	2.7	⋯	w			5077 ± 2	126 ± 4
84	NGC 612	Sy 2	SOAR/GMAN	2.7	⋯	w			9137 ± 12	336 ± 20
87	ESO 297-18	Sy 2	SOAR/GMAN	2.7	⋯	w			7864 ± 8	141 ± 9
88	LEDA 138434	Sy 1.9	Palomar/DBSP	4.1	4.9	n			22,206 ± 13	123 ± 18
92	LEDA 1656658	Sy 1.9	Palomar/DBSP	4.1	4.9	n			21,281 ± 18	209 ± 19
96	MCG-1-5-47	Sy 2	Palomar/DBSP	4.8	3.4	n			5662 ± 9	85 ± 12
101	UGC 01479	Sy 2	Palomar/DBSP	4.1	4.9	n			5029 ± 6	142 ± 9
112	Arp 318	Sy 2	APO/SDSS	3.0	⋯	n	3963 ± 2	182 ± 3	3971 ± 3	168 ± 4
123	VII Zw 232	Sy 2	Palomar/DBSP	4.8	6.5	n	18,937 ± 16	206 ± 17		
140	NGC 1052	Sy 2	Gemini/GMOS	4.8	⋯	n	1560 ± 3	218 ± 4		
145	2MFGC 02171	Sy 2	Palomar/DBSP	4.8	6.5	n			10,720 ± 11	131 ± 15
149	LEDA 89928	Sy 2	Palomar/DBSP	2.3	1.8	n	17,803 ± 17	170 ± 20	17,767 ± 14	256 ± 14
151	LEDA 166445	Sy 2	Palomar/DBSP	4.1	4.9	n			4690 ± 8	160 ± 12
153	NGC 1125	Sy 2	Palomar/DBSP	4.1	4.9	n	3435 ± 9	103 ± 12	3334 ± 5	127 ± 5

Note. Column descriptions are the same as in Table 2.

(This table is available in its entirety in machine-readable form.)

Appendix D
Comparison of the DR1 and DR2 Velocity Dispersions

In comparing with the DR1, we limit our sample to only the sources with $\Delta\sigma_* < 20$ km s^{-1}, whereas the DR1 included fits up to 50 km s^{-1} to better understand any systematic offsets. Outside of the SDSS sample and a small number of Palomar/DBSP and Gemini/GMOS spectra that are included in this study, we note that nearly all of the DR1 sources were reobserved as part of the higher spectral resolution DR2 survey. This limits the sample to 29 Sy 1.9 and 89 Sy 2 galaxies that were measured in both the DR1 and the current sample. Overall, we find that there is a median offset in the DR1 of 9.6 and 6.6 km s^{-1} for Sy 1.9 and Sy 2, respectively (e.g., $|\sigma_{\rm DR1} - \sigma_{\rm best}|$). These offsets correspond to median offsets of 0.11 and 0.08 dex for Sy 1.9 and Sy 2 in measured SMBH, respectively (or a median of 0.09 dex for the combined sample). This systematic difference is relatively small compared to the expected typical systematic error (e.g., 0.3–0.5 dex), so we do not expect it to affect any specific DR1 studies that were based on the entire sample. However, there are outliers in specific samples and the Sy 1.9 tend to show increased offsets.

A useful test of the effect of the new templates, changed fitting regions, and updated pPXF software applied is provided in the overlapping spectra in the SDSS. There are 46 Sy 2 and 17 Sy 1.9 overlapping within the DR1 and DR2. A comparison of the velocity dispersion measurements from the DR1 and DR2 for the SDSS samples is shown in Figure 16. The DR1 fit the entire 3900–7000 Å region for the SDSS spectra, whereas the DR2 was limited to 3880–5550 Å. There is a systematic shift in both Sy 2 and Sy 1.9, with the velocity dispersion measurements being somewhat larger in the DR1 than the DR2 and Sy 1.9 showing larger offsets and scatter. Some of the larger scatter is likely from the fact that Sy 1.9 has larger typical measurement errors than Sy 2 (e.g., for the DR1, the median 1σ error is 10 and 6 km s^{-1}, respectively). Among Sy 2, the median offset ($|\sigma_{\rm DR1} - \sigma_{\rm best}|$) is 4.0 km s^{-1}. Among Sy 1.9, the median offset is larger at 14 km s^{-1}.

We then expand our comparison of our current work to the other DR1 samples that are not in the current study. This includes spectra taken from the Perkins 1.8 m telescope and DeVeny Spectrograph at the Lowell Observatory and the CTIO 1.5 m RC spectrograph, as well as archival optical spectra obtained as part of the final data release for the 6dF Galaxy Survey (Jones et al. 2009). There are six systems observed with other telescopes that were significant outliers (e.g., >30 km s^{-1} beyond 1σ error bars) between the DR1 and DR2, which includes four Sy 1.9 and two Sy 2. The outliers showed differences in velocity dispersion between 38 and 85 km s^{-1} corresponding to offsets in SMBH mass of 0.2–0.6 dex. All of the six outliers were at higher redshifts ($z > 0.059$) and had high AGN luminosities ($L_{\rm bol} > 10^{45}$ erg s^{-1}) and larger errors (12–20 km s^{-1}) than typical of the sample. The Sy 1.9 outliers all show evidence of extremely broad lines that were not properly masked in the original DR1 fitting procedure,

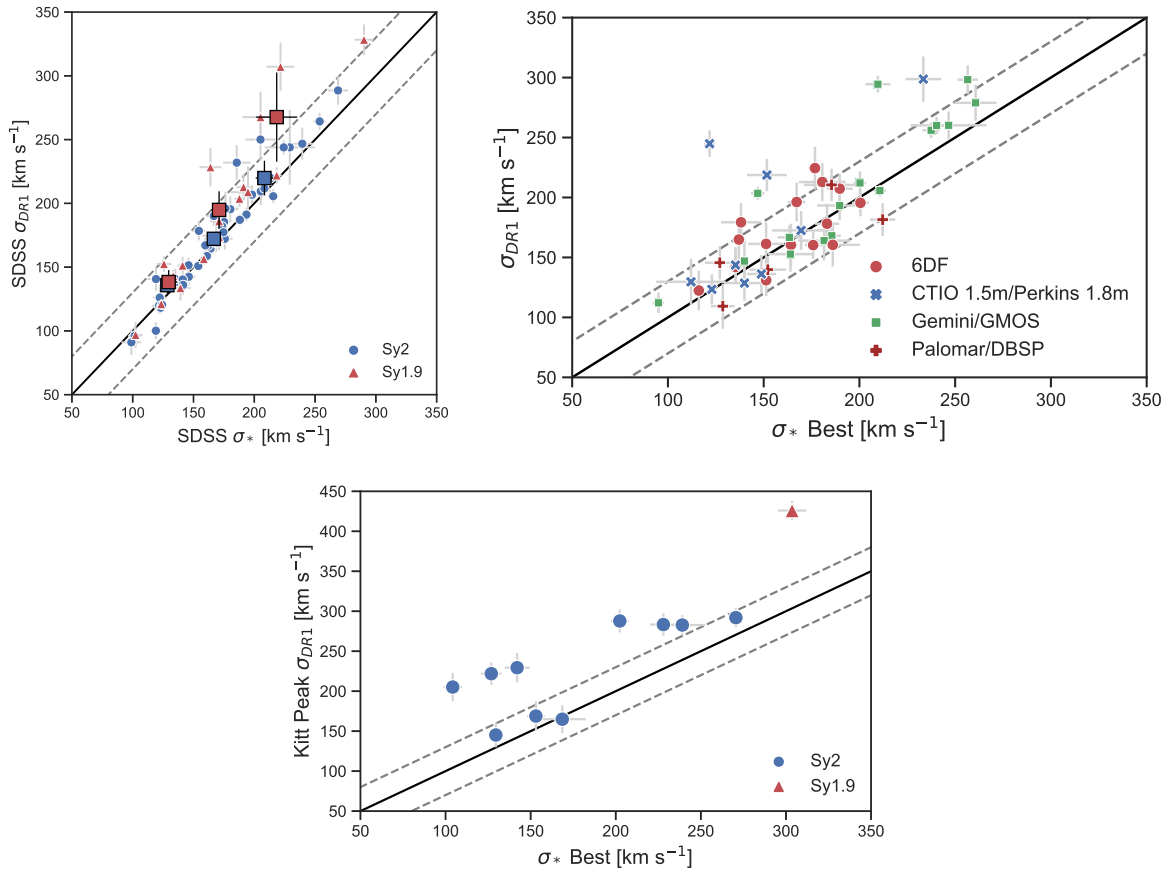

Figure 16. Comparison between different velocity dispersion measurements. In all panels, Sy 1.9 (with broad Hα) is shown with red triangles, and Sy 2 is shown with blue circles. Error bars (at 1σ) are shown in gray. A solid black line indicates the one-to-one relation, with dashed gray lines indicating offsets of 30 km s^{-1}. Top left: comparison between the velocity dispersion measurements from the SDSS for the DR1 and DR2 for DR1 measurements with $\Delta\sigma_* < 20$ km s^{-1}. Top right: comparison between the velocity dispersion measurements from other DR1 samples and the current best measurements. Bottom: comparison between the velocity dispersion measurements from the KP DR1 samples where there is a significant fraction of outliers.

which excluded regions of 3200 km s^{-1} around Hα. Three of the systems show double-peaked and/or asymmetric broad lines (ID 522, 715, and 817), which are rare in the BAT sample. The final system (ID = 785) shows a very broad line (Hα FWHM = 7800 km s^{-1}). The two outlier Sy 2 systems are likewise unique, with the presence of strong outflows or double-peaked narrow emission lines. Recent, optical integral field spectroscopy with the Gemini North Telescope (Couto et al. 2020) for 4C+29.30 (BAT ID = 426) indicated a large southern knot 1″ south of the nucleus (and hence in the 3″ SDSS fiber), which also presents high velocity dispersions (∼250 km s^{-1}) attributed to an outflow. The other Sy 2 outlier, SDSS J000911.58–003654.7 (BAT ID = 7), shows double-peaked narrow emission lines and five nearby galaxies within 30″ at similar redshift (<500 km s^{-1}), indicative of a galaxy group.

Finally, we examine a DR1 sample from the 2.1 m telescope at the Kitt Peak (KP) national observatory with the GoldCam spectrograph. It is clear that the KP sample specifically shows >30 km s^{-1} outliers for the majority of the sample. The outliers all appear above 200 km s^{-1}, so a possible reason is a significant underestimation of the instrumental resolution. The median offset is 55 km s^{-1}, corresponding to 0.41 dex in SMBH mass.

In summary, while the median systematic offset with the DR1 is small (e.g., 9.6 and 6.6 km s^{-1} for Sy 1.9 and Sy 2, respectively), there is a population of outliers that bias the distributions. We find that Sy 1.9 shows larger systematic offsets in the DR1, likely due to AGN contamination. This is seen in the outliers tending to have very broad lines and be double-peaked sources. As the AGN broad Hα and continuum emission scales with the hard X-ray emission (e.g., Mejía-Restrepo et al. 2022), the host galaxy absorption features are likely diluted in these systems, leading to erroneously large measurements compared to the DR2 measurements, which did not fit the Hα region. The small offset among Sy 2 is puzzling but may be related to the lower spectral resolution of the DR1 sample. Finally, with the higher-quality observations, we can see that the KP sample has large systematic errors and should not be used. As the DR2 observations presented here are of much higher S/N and spectral resolution, they should be used in place of these measurements.

Appendix E
Velocity Dispersion Failures in the DR2

A list of the AGN for which we were unable to measure velocity dispersions is provided in Table 8.

Table 8
DR2 Velocity Dispersion Failures

BAT ID	Counterpart	Reason	A_V (mag)	DR2 Type	z	Best Spectra
(1)	(2)	(3)	(4)	(5)	(6)	(7)
5	2MASX J00040192+7019185	GalExt	2.67	Sy 1.9	0.0957	Palomar/DBSP
18	2MASX J00331831+6127433	GalExt	3.72	Sy 1.9	0.1042	Palomar/DBSP
119	2MASS J02162672+5125251	GalExt	0.59	Sy 2	0.4223	Palomar/DBSP
172	2MASX J03181899+6829322	GalExt	2.29	Sy 1.9	0.0906	Palomar/DBSP
173	NGC 1275	Emission	0.5	Sy 1.9	0.0168	Palomar/DBSP
249	LEDA 1797736	GalExt	3.5	Sy 2	0.061	Palomar/DBSP
285	2MASX J05325752+1345092	GalExt	2.51	Sy 1.9	0.024	VLT/X-Shooter
315	IRAS 05581+0006	GalExt	2.26	Sy 1.9	0.1144	Magellan/MagE
360	2MASX J07091407–3601216	GalExt	2.2	Sy 2	0.1107	VLT/X-Shooter
367	1RXS J072352.4–080623	GalExt	0.93	Sy 1.9	0.1449	Palomar/DBSP
372	1RXS J072720.8–240629	GalExt	3.1	Sy 1.9	0.1219	VLT/X-Shooter
381	3C 184.1	lowSN	0.09	Sy 1.9	0.1183	Palomar/DBSP
433	SWIFT J085429.35–082428.6	lowSN	0.09	Sy 2	0.1884	VLT/X-Shooter
441	2MASX J09023729–4813339	GalExt	5.18	Sy 2	0.0392	VLT/X-Shooter
476	CXO J095220.1–623234	GalExt	0.93	Sy 1.9	0.2521	VLT/X-Shooter
494	SDSS J102103.08–023642.6	lowSN	0.12	Sy 2	0.2936	VLT/X-Shooter
505	SDSS J103315.71+525217.8	lowSN	0.06	Sy 2	0.1404	Palomar/DBSP
516	2MASS J10445192–6025115	GalExt	9.55	Sy 2	0.047	Nospec
533	2MASX J11140245+2023140	lowSN	0.06	Sy 2	0.0271	Palomar/DBSP
639	2MASX J12475784–5829599	GalExt	1.86	Sy 2	0.0276	VLT/X-Shooter
661	2MASX J13103701–5626551	GalExt	1.98	Sy 2	0.1142	VLT/X-Shooter
692	4U 1344-60	GalExt	9.02	Sy 1.9	0.0128	VLT/X-Shooter
703	Mrk 463E	Emission	0.09	Sy 1.9	0.0501	Palomar/DBSP
745	2MASX J14545815+8554589	lowSN	0.53	Sy 2	0.112	Palomar/DBSP
747	LEDA 3085605	GalExt	2.54	Sy 2	0.0187	VLT/X-Shooter
896	1RXS J173728.0–290759	GalExt	7.1	Sy 1.9	0.0218	VLT/X-Shooter
929	2MASS J17485512–3254521	GalExt	5.24	Sy 1.9	0.0207	Nospec
976	CXO J182557.5–071022	GalExt	6.14	Sy 2	0.037	VLT/X-Shooter
1073	2MASX J20183871+4041003	GalExt	10.6	Sy 2	0.0145	Palomar/DBSP
1075	1RXS J202400.8–024527	lowSN	0.22	Sy 1.9	0.1375	VLT/X-Shooter
1096	SWIFT J210001.06+430209.6	GalExt	4.09	Sy 2	0.066	Palomar/DBSP
1110	4C+50.55	GalExt	7.53	Sy 1.9	0.0154	Palomar/DBSP
1191	2MASX J23203662+6430452	GalExt	5.15	Sy 1.9	0.0729	Palomar/DBSP
1207	CXO J235221.9+584531	GalExt	3.97	Sy 2	0.1629	Palomar/DBSP

Note. The columns are as follows. (1) Catalog ID from BAT survey. (2) Host galaxy. (3) Reason for failure. GalExt = failure due to being within the Galactic plane and having high optical extinction, lowSN = low S/N typically because $z > 0.1$, Emission = Galaxy spectra was dominated by strong and broad emission lines that contaminated the absorption lines, Nospec = no suitable high-resolution spectra were available due to the very high levels of extinction. (4) Visual extinction due to Milky Way foreground dust using the maps of Schlegel et al. (1998) and the extinction law derived by Cardelli et al. (1989). (5) AGN type based on optical spectroscopy including Sy 1.9 (narrow Hβ and broad Hα) and Sy 2 (narrow Hβ and Hα) from Koss et al. (2022b). (6) Redshift based on emission lines from Koss et al. (2022b). (7) Best available spectra in the DR2 based on telescope diameter and spectral resolution.

ORCID iDs

Michael J. Koss https://orcid.org/0000-0002-7998-9581
Benny Trakhtenbrot https://orcid.org/0000-0002-3683-7297
Claudio Ricci https://orcid.org/0000-0001-5231-2645
Kyuseok Oh https://orcid.org/0000-0002-5037-951X
Franz E. Bauer https://orcid.org/0000-0002-8686-8737
Daniel Stern https://orcid.org/0000-0003-2686-9241
Turgay Caglar https://orcid.org/0000-0002-9144-2255
Jakob S. den Brok https://orcid.org/0000-0002-8760-6157
Richard Mushotzky https://orcid.org/0000-0002-7962-5446
Federica Ricci https://orcid.org/0000-0001-5742-5980
Julian E. Mejía-Restrepo https://orcid.org/0000-0001-8450-7463
Isabella Lamperti https://orcid.org/0000-0003-3336-5498
Ezequiel Treister https://orcid.org/0000-0001-7568-6412
Rudolf E. Bär https://orcid.org/0000-0001-5481-8607
Meredith C. Powell https://orcid.org/0000-0003-2284-8603
George C. Privon https://orcid.org/0000-0003-3474-1125
Rogério Riffel https://orcid.org/0000-0002-1321-1320
Alejandra F. Rojas https://orcid.org/0000-0003-0006-8681
Kevin Schawinski https://orcid.org/0000-0001-5464-0888
C. Megan Urry https://orcid.org/0000-0002-0745-9792

References

Ananna, T. T., Weigel, A. K., Trakhtenbrot, B., et al. 2022, ApJS, 260, 32
Astropy Collaboration, A., Robitaille, T. P., Tollerud, E. J., et al. 2013, A&A, 558, A33
Baldassare, V. F., Dickey, C., Geha, M., & Reines, A. E. 2020, ApJL, 898, L3
Baldwin, J. A., Phillips, M. M., & Terlevich, R. 1981, PASP, 93, 5
Baumgartner, W. H., Tueller, J., Markwardt, C. B., et al. 2013, ApJS, 207, 19
Belfiore, F., Westfall, K. B., Schaefer, A., et al. 2019, AJ, 158, 160

Bellovary, J. M., Holley-Bockelmann, K., Gültekin, K., et al. 2014, MNRAS, 445, 2667
Bentz, M. C., Walsh, J. L., Barth, A. J., et al. 2009, ApJ, 705, 199
Boardman, N. F., Weijmans, A.-M., van den Bosch, R., et al. 2016, MNRAS, 460, 3029
Boardman, N. F., Weijmans, A.-M., van den Bosch, R., et al. 2017, MNRAS, 471, 4005
Brandt, W. N., & Hasinger, G. 2005, ARA&A, 43, 827
Caglar, T., Burtscher, L., Brandl, B., et al. 2020, A&A, 634, A114
Capetti, A., Marconi, A., Macchetto, D., & Axon, D. 2005, A&A, 431, 465
Cappellari, M. 2017, MNRAS, 466, 798
Cappellari, M., & Emsellem, E. 2004, PASP, 116, 138
Cardelli, J. A., Clayton, G. C., & Mathis, J. S. 1989, ApJ, 345, 245
Carnall, A. 2021, SpectRes: Simple spectral resampling, Astrophysics Source Code Library, ascl:2104.019
Clemens, J. C., Crain, J. A., & Anderson, R. 2004, Proc. SPIE, 5492, 331
Cohn, J. H., Walsh, J. L., Boizelle, B. D., et al. 2021, ApJ, 919, 77
Couto, G. S., Storchi-Bergmann, T., Siemiginowska, A., Riffel, R. A., & Morganti, R. 2020, MNRAS, 497, 5103
Davis, T. A. 2014, MNRAS, 443, 911
Davis, T. A., Bureau, M., Onishi, K., et al. 2017, MNRAS, 468, 4675
den Brok, J., Koss, M. J., Trakhtenbrot, B., et al. 2022, ApJS, 261, 7
Emmanoulopoulos, D., McHardy, I. M., Vaughan, S., & Papadakis, I. E. 2016, MNRAS, 460, 2413
Fabian, A. 2012, ARA&A, 50, 455
Falcon-Barroso, J., Lyubenova, M., van de Ven, G., et al. 2017, A&A, 597, A48
Gannon, J. S., Forbes, D. A., Romanowsky, A. J., et al. 2020, MNRAS, 495, 2582
Garcia-Rissmann, A., Vega, L. R., Asari, N. V., et al. 2005, MNRAS, 359, 765
Gonneau, A., Lyubenova, M., Lançon, A., et al. 2020, A&A, 634, A133
Graham, A. W. 2008, PASA, 25, 167
Greene, J. E., & Ho, L. C. 2005, ApJ, 627, 721
Greene, J. E., & Ho, L. C. 2006, ApJ, 641, 117
Greene, J. E., Seth, A., Kim, M., et al. 2016, ApJL, 826, L32
Greene, J. E., Strader, J., & Ho, L. C. 2020, ARA&A, 58, 257
Grier, C. J., Martini, P., Watson, L. C., et al. 2013, ApJ, 773, 90
Gultekin, K., Richstone, D. O., Gebhardt, K., et al. 2009, ApJ, 698, 198
Hickox, R. C., & Alexander, D. M. 2018, ARA&A, 56, 625
Ho, L. C., Greene, J. E., Filippenko, A. V., & Sargent, W. L. W. 2009, ApJS, 183, 1
Ho, L. C., & Kim, M. 2009, ApJS, 184, 398
Hunter, J. D. 2007, CSE, 9, 90
Johnson, S. C. 1967, Psychometrika, 32, 241
Jones, D. H., Read, M. A., Saunders, W., et al. 2009, MNRAS, 399, 683
Jorgensen, I., Franx, M., & Kjaergaard, P. 1995, MNRAS, 276, 1341
Kakkad, D., Sani, E., Rojas, A. F., et al. 2022, MNRAS, 511, 2105
Kewley, L. J., Heisler, C. A., Dopita, M. A., & Lumsden, S. 2001, ApJS, 132, 37
Kong, M., & Ho, L. C. 2018, ApJ, 859, 116
Kormendy, J., & Ho, L. C. 2013, ARA&A, 51, 511
Koss, M., Mushotzky, R., Baumgartner, W., et al. 2013, ApJL, 765, L26
Koss, M., Mushotzky, R., Treister, E., et al. 2011b, ApJL, 735, L42
Koss, M., Mushotzky, R., Treister, E., et al. 2012, ApJL, 746, L22
Koss, M., Mushotzky, R., Veilleux, S., & Winter, L. 2010, ApJL, 716, L125
Koss, M., Mushotzky, R., Veilleux, S., et al. 2011a, ApJ, 739, 57
Koss, M., Ricci, C., Trakhtenbrot, B., et al. 2022b, ApJS, 261, 2
Koss, M., Trakhtenbrot, B., Ricci, C., et al. 2017, ApJ, 850, 74
Koss, M., Trakhtenbrot, B., Ricci, C., et al. 2022a, ApJS, 261, 1
Koss, M. J., Assef, R., Balokovic, M., et al. 2016a, ApJ, 825, 85
Koss, M. J., Blecha, L., Bernhard, P., et al. 2018, Natur, 563, 214
Koss, M. J., Glidden, A., Balokovic, M., et al. 2016b, ApJL, 824, L4
Koss, M. J., Romero-Cañizales, C., Baronchelli, L., et al. 2015, ApJ, 807, 149
Koss, M. J., Strittmatter, B., Lamperti, I., et al. 2021, ApJS, 252, 29
Kuo, C. Y., Braatz, J. A., Condon, J. J., et al. 2011, ApJ, 727, 20
Marsden, C., Shankar, F., Ginolfi, M., & Zubovas, K. 2020, FrP, 8, 61
Martin-Navarro, I., & Mezcua, M. 2018, ApJL, 855, L20
McConnell, N. J., & Ma, C.-P. 2013, ApJ, 764, 184
Medling, A. M., Ammons, S. M., Max, C. E., et al. 2011, ApJ, 743, 32
Mejía-Restrepo, J., Koss, M. J., Trakhtenbrot, B., et al. 2022, ApJS, 261, 5
Merritt, D. 1997, AJ, 114, 228
Nelson, C. H., & Whittle, M. 1995, ApJS, 99, 67
Neumayer, N. 2010, PASA, 27, 449
Oh, K., Koss, M., Markwardt, C. B., et al. 2018, ApJS, 235, 4
Oh, K., Koss, M. J., Ueda, Y., et al. 2022, ApJS, 261, 4
Oh, K., Sarzi, M., Schawinski, K., & Yi, S. K. 2011, ApJS, 195, 13
Osterbrock, D. E., & Fulbright, J. P. 1996, PASP, 108, 183
Osterbrock, D. E., Shaw, R. A., & Veilleux, S. 1990, ApJ, 352, 561
Pfeifle, R. W., Ricci, C., Boorman, P. G., et al. 2022, ApJS, 261, 3
Reines, A. E., Greene, J. E., & Geha, M. 2013, ApJ, 775, 116
Ricci, C., Trakhtenbrot, B., Koss, M. J., et al. 2017, ApJS, 233, 17
Ricci, C., Ueda, Y., Koss, M. J., et al. 2015, ApJL, 815, L13
Ricci, F., Treister, E., Bauer, F. E., et al. 2022, ApJS, 261, 8
Riffel, R. A., Ho, L. C., Mason, R., et al. 2015, MNRAS, 446, 2823
Ryan, G., & MacFadyen, A. 2017, ApJ, 835, 199
Sahu, N., Graham, A. W., & Davis, B. L. 2019a, ApJ, 876, 155
Sahu, N., Graham, A. W., & Davis, B. L. 2019b, ApJ, 887, 10
Scharwachter, J., McGregor, P. J., Dopita, M. A., & Beck, T. L. 2013, MNRAS, 429, 2315
Schlegel, D. J., Finkbeiner, D. P., & Davis, M. 1998, ApJ, 500, 525
Scott, N., van de Sande, J., Croom, S. M., et al. 2018, MNRAS, 481, 2299
Shankar, F., Bernardi, M., Richardson, K., et al. 2019, MNRAS, 485, 1278
Shankar, F., Bernardi, M., & Sheth, R. K. 2017, MNRAS, 466, 4029
Smith, M. D., Bureau, M., Davis, T. A., et al. 2021, MNRAS, 503, 5984
Staveley-Smith, L., Norris, R. P., Chapman, J. M., et al. 1992, MNRAS, 258, 725
Stickley, N. R., & Canalizo, G. 2012, ApJ, 747, 33
Straatman, C. M. S., van der Wel, A., Bezanson, R., et al. 2018, ApJS, 239, 27
Tadhunter, C., Marconi, A., Axon, D., et al. 2003, MNRAS, 342, 861
Thomas, D., Steele, O., Maraston, C., et al. 2013, MNRAS, 431, 1383
Tran, H. D., Cohen, M. H., & Villar-Martin, M. 2000, AJ, 120, 562
Treister, E., Privon, G. C., Sartori, L. F., et al. 2018, ApJ, 854, 83
van den Bosch, R. C. E., Gebhardt, K., Gültekin, K., Yildirim, A., & Walsh, J. L. 2015, ApJS, 218, 10
van der Walt, S., Colbert, S. C., & Varoquaux, G. 2011, CSE, 13, 22
Vasudevan, R. V., & Fabian, A. C. 2009, MNRAS, 392, 1124
Vazdekis, A., Ricciardelli, E., Cenarro, A. J., et al. 2012, MNRAS, 424, 157
Veilleux, S., & Osterbrock, D. E. 1987, ApJS, 63, 295
Vernet, J., Dekker, H., D'Odorico, S., et al. 2011, A&A, 536, A105
Walsh, J. L., van den Bosch, R. C. E., Barth, A. J., & Sarzi, M. 2012, ApJ, 753, 79
Westfall, K. B., Cappellari, M., Bershady, M. A., et al. 2019, AJ, 158, 231
Wold, M., Lacy, M., Käufl, H. U., & Siebenmorgen, R. 2006, A&A, 460, 449
Woo, J.-H., Schulze, A., Park, D., et al. 2013, ApJ, 772, 49
Yuan, F., & Narayan, R. 2014, ARA&A, 52, 529